Extended Layerwise method for laminated composite plates with multiple delaminations and transverse cracks

D. H. Li · X. Zhang* · K. Y. Sze · Y. Liu

Received: date / Accepted: date

Abstract In this paper, the extended layerwise method (XLWM), which was developed for laminated composite beams with multiple delaminations and transverse cracks [1], is extended to laminated composite plates. The strong and weak discontinuous functions along the thickness direction are adopted to simulate multiple delaminations and interlaminar interfaces, respectively, whilst transverse cracks are modeled by the extended finite element method (XFEM). The interaction integral method and maximum circumferential tensile criterion are used to calculate the stress intensity factor (SIF) and crack growth angle, respectively. The XLWM for laminated composite plates can accurately predicts the displacement and stress fields near the crack tips and delamination fronts. The thickness distribution of SIF and thus the crack growth angles in different layers can be obtained. These information cannot be predicted by using other existing shell elements enriched by XFEM. Several numerical examples are studied to demonstrate the capabilities of the XLWM in static response analyses, SIF calculations and crack growth predictions.

Keywords Composite laminated plates; Layerwise theory; Delamination; Transverse crack.

D. H. Li
School of Aerospace Engineering, Tsinghua University, Beijing 100084, China
E-mail: lidinghe@163.com *Present address:College of Aeronautical Engineering, Civil Aviation University of China, Tianjin 300300, China* of F. Author

X. Zhang*
School of Aerospace Engineering, Tsinghua University, Beijing 100084, China
E-mail: xzhang@tsinghua.edu.cn

K. Y. Sze
Department of Mechanical Engineering, The University of Hong Kong, Pokfulam, Hong Kong, China

Y. Liu
School of Aerospace Engineering, Tsinghua University, Beijing 100084, China

Published in: Computational Mechanics 58:657–679 (2016)
DOI 10.1007/s00466-016-1310-2

Highlight:

1. XLWM can accurately predict the displacement and stress fields of the crack tip and delamination front in laminated composite plates;
2. The thickness distribution of the SIF can be calculated and the predicted crack growth angles are different for each mathematic layer;
3. When these nodes are very close to the crack surface as the crack grows, the present local remeshing scheme can shift these nodes without scarifying the mesh quality.

1 Introduction

Due to the outstanding designability, high strength/stiffness-to-weight ratio and excellent resistance to fatigue and corrosion, carbon fiber reinforced polymer matrix composites have been increasingly applied in various fields. Under different loading conditions, the layered and orthotropic characteristics would result in different failure modes in the composites. In general, failure modes of composites include delamination, matrix cracking, fibre breakage and fibre/matrix debonding whilst the first two modes are dominating due to the high tensile strength of the fiber. For instance, fiber breakage is generally very limited and confined to the region under and near the contact area between the impactor and composite laminates in low velocity impact of laminated composite structures [2]. To model matrix cracks and delaminations, damage mechanics and fracture mechanics were usually used [3–10]. Although there are a lot of investigations on the static response, free vibration and buckling of laminated composite structures with delaminations or matrix cracks, only a few of them consider multiple delaminations and matrix cracks [11–15].

For problems with material and geometric discontinuities, the extended finite element method (XFEM) was developed based on the conventional FEM and the concept of partition of unity [16–20]. This method was generalized to model transverse cracks and crack growth in plates and shell [21–24]. Later on, it was extended to the delamination and in-plane crack of composite structures. Remmers [25] presented a new finite element method for simulating delamination growth in thin-layered composite structures based on a solid-like shell element and the partition-of-unity property of the element shape functions. For the problem of interfacial cracks between dissimilar materials, XFEM was extended by using the orthotropic enrichment functions [26]. Hettich and Ramm [27] carried out a detailed geometric modeling of multi-phase materials and a local mechanical modeling of material interfaces and interfacial failure for multi-phase materials. The mechanical modeling of material interfaces and interfacial cracks is accomplished by XFEM without any crack tip enrichment. Nagashima and Suemasu [28] applied XFEM to stress analysis of delaminated

composite plate. To model the delamination, nodes on above and below the delamination were enriched. Curiel Sosa and Karapurath [29] applied the XFEM to simulating delamination in the fibre metal laminates. Their study considered a double cantilever plate with mode I crack. Development of the orthotropic crack-tip enrichment functions for the composite materials are reported in a series of works [30–32]. Motamedi and Mohammadi [33,34] studied the dynamic crack stability and propagation in composites based on static and dynamic orthotropic crack-tip enrichment functions. Although, remarkable progress on the application of XFEM in composite damages analysis has been achieved in the last decade, two important aspects should be improved. Firstly, existing shell elements methods enriched by XFEM can only deal with the through-thickness cracks yet many the matrix cracks are restricted to the single layers around the impact contact zone[2]. Secondly, the existing shell elements enriched by XFEM were applied to model either cracks or delaminations. No work has been reported for the typical damage pattern which include matrix cracks and delaminations simultaneously. In particular, the damage zone induced by low velocity impact contains complex three-dimensional cracks with layered characteristics. Since it is very difficult to apply XFEM directly to deal with complex three-dimensional crack, one cannot just rely on XFEM to solve this complex problem.

Recently, the Heaviside step-function was introduced into the displacement field along the thickness direction for modeling the delamination [35–40]. In those methods, the delaminations were modeled by jump discontinuous conditions across the interlaminar interfaces. Thus, the displacements on adjacent layers remain independent, allowing for separation and slippage.

Therefore,if the transverse cracks are perpendicular to each layer, one can convert the complex three-dimensional damage with layered characteristics to two two-dimensional cracks (delaminations and transverse cracks) by using an appropriate displacement assumption along thickness direction. Hence, the multiple delaminations can be simulated by the jump discontinuous functions in the thickness direction and the in-plane transverse cracks inside each ply can be modeled independently by XFEM.

The displacement field employed in Layerwise theories can be used to calculate the three-dimensional stresses and strains of each mathematical layer. Particularly, the finite element model of the displacement-based full layerwise theory of Reddy is equivalent to the displacement-based 3D continuum finite element model [41]. Thus, it would be suitable to simulate the complex three-dimensional crack with layered characteristics by combining with XFEM. In our previous work [1], an extended layerwise method (XLWM) was developed by using the layerwise theory and XFEM for laminated composite beams with multiple delaminations and transverse cracks. In the displacement field of XLWM, the nodes in the thickness direction are located at the mid-surface of each layer, top surface and bottom surface of whole composite beams. The displacement field contains the linear Lagrange interpolation functions, the one-dimensional weak discontinuous function and strong discontinuous function. The strong and weak discontinuous functions are applied to model the

displacement discontinuity induced by delaminations and the strain discontinuity induced by the interlaminar interface, respectively. Because the nodes in the thickness direction are located at the mid-surface of each layer, the XLWM can be conveniently employed to deal with the transverse cracks.

In the present work, the XLWM is extended to the laminated composite plates for static responses analysis, SIF calculation and transverse crack arbitrary growth prediction. The rest of this paper is organized as follows. In the next section, the displacement field for the laminated composite plates is introduced. The in-plane displacement approximation used to model the laminated composite plate with multiple delaminations and/or transverse cracks as well as the level set function and the crack-tip enrichment functions used to represent the transverse cracks are described. In Sections 3 and 4, the Hamilton's principle, Euler-Lagrange equations and constitutive equations are established for the XLWM of laminated composite plates. The governing equations for laminated plates with multiple delaminations and/or transverse cracks are developed in Section 5. The SIF calculation method and transverse crack propagation criterion are presented in Section 6. As the transverse crack grows, some nodes would be very close to the crack surface. In this light, a local remeshing scheme will be presented in Section 7. In Section 8, several numerical examples for demonstrating the capability of the XLWM in static responses analysis, SIF calculation and crack arbitrary growth predication are presented. Conclusions are drawn in Section 9.

2 Displacements field and in-plane displacements discretization

2.1 Displacements field

In our previous work [1], in order to model the displacement discontinuity of delaminations based on the strong discontinuous functions, nodes along the thickness direction are placed at the top surface, bottom surface and mid-surface of each layer. This node distribution is also necessary for the simulation of transverse cracks. However, the weak discontinuous function is needed in this displacement field to model the strain discontinuity resulted from the interlaminar interfaces.

For plate with multiple delaminations, the displacements field is similar to that in our previous work [1], see Figure 1. In the Figure, h_k is the thickness of the k-th layer and z_k is the thickness coordinate of the interface between k-th layer and $(k-1)$-th layer, the numbers on the left side denote the nodes along the thickness direction, the numbers on the right side denote the interfaces between the N layers in the plate.

The present layerwise concept is very general in the sense that the number of mathematical layers can be greater than, equal to or less than the number of the material layers. Within a mathematical layer, the material is homogeneous. Adjacent material layers of the same fiber angle may be more efficiently modelled as a single mathematical layer. On the other hand, a material lay-

er can be modelled by multiple mathematical layers for higher resolution, if necessary. Figure 1 shows that the numbers of the nodal freedoms and the nodeless freedoms for interfaces are $N + 2$ and N, respectively.

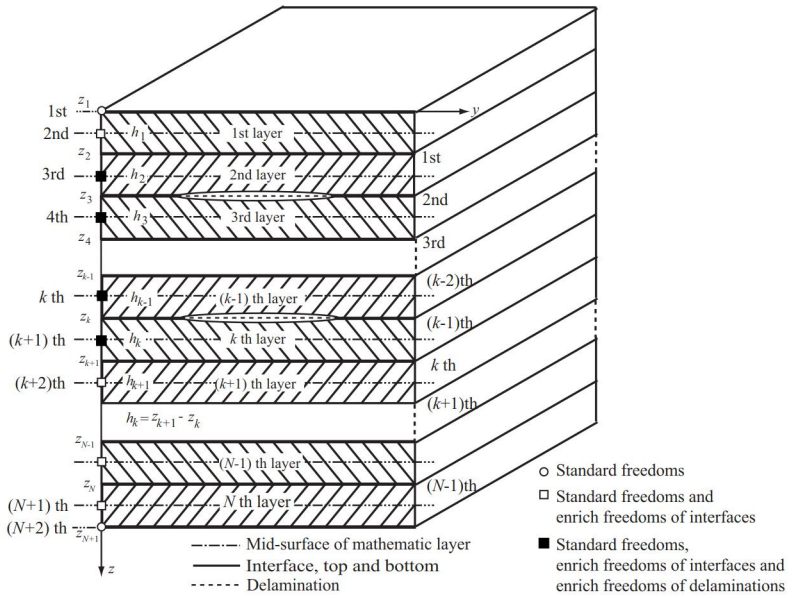

Fig. 1 A N-ply composite plates with multiple delaminations

The displacements at point (x, y, z) in the composite laminated plate with multiple delaminations can be expressed as

$$u_\alpha(x,y,z,t) = \sum_{k=1}^{N+2} \phi_k(z) u_{\alpha ik}(x,y,t) + \sum_{k=1}^{N_D} \Xi_k(z) u_{\alpha lk}(x,y,t) + \sum_{k=2}^{N+1} \Theta_k(z) u_{\alpha rk}(x,y,t) \tag{1}$$

where N_D is the number of nodes to be enriched for modelling the delaminations; $\alpha = 1, 2, 3$ denotes the components in the x, y and z directions; $u_{\alpha ik}$, $u_{\alpha lk}$ and $u_{\alpha rk}$ are the nodal freedom, the additional nodal freedom to model displacements discontinuity induced by delaminations and the additional nodal freedom to model strains discontinuity induced by interface between the layers, respectively; the subscripts i, l and r denote the standard nodal freedom, the additional nodal freedom for delaminations and the additional nodal freedom for interfaces, respectively; ϕ_k is the linear Lagrange interpolation functions along the thickness direction of the laminated composite plate, see Figure 2(a): $\Theta_k = \phi_k(z)\chi_k(z)$ is the weak discontinuous shape function used to model the strains discontinuity in the interface between the layers (see Figure 2(b)) and $\chi_k(z)$ is the one-dimensional signed distance function; $\Xi_k = \phi_k(z)H_k(z)$ is the shape function used to model delaminations and $H_k(z)$ is the one-dimensional

Heaviside function, see Figure 2(c). The detailed expressions of ϕ_k, Θ_k and Ξ_k can be found in the Appendix A. Therefore, in the proposed XLWM, the nodal freedoms are located at the top surface, bottom surface and mid-surface of each mathematical layer. The additional nodal freedoms to model strains discontinuity are located at the mid-surface of each mathematical layer. The additional nodal freedoms to model displacements discontinuity induced by delaminations are located at the mid-surface of the mathematical layers nearby the delamination. The location of the freedoms also can be found in Figure 1.

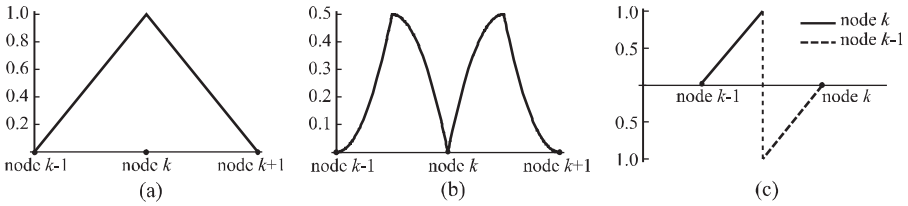

Fig. 2 Shape functions in the displacement field. (a) ϕ_k; (b) $\Theta_k = \phi_k(z)\chi_k(z)$; (c) $\Xi_k = \phi_k(z)H_k(z)$.

Let

$$\Phi_{ik} = \phi_k(z),\ \Phi_{lk} = \Xi_k(z),\ \Phi_{rk} = \Theta_k(z) \tag{2}$$

Using the Einstein summation convention for repeated indexes, Eq.(1) can be expressed as

$$u_\alpha(x, y, z, t) = \Phi_{\zeta k}(z) u_{\alpha\zeta k}(x, y, t),\ \zeta = i,\ l,\ r \tag{3}$$

where $k \in [1, N+2], [1, N_D]$ and $[2, N+1]$ for $\zeta = i, l$ and r, respectively.

If there is no delaminations, the displacement field can be simplified to

$$u_\alpha(x, y, z, t) = \Phi_{\zeta k}(z) u_{\alpha\zeta k}(x, y, t),\ \zeta = i,\ r \tag{4}$$

In the displacement-based full layerwise theory of Reddy [41], the layerwise continuous functions, such as the one-dimensional Lagrange interpolation functions along the thickness direction, are used to develop the displacement field of the laminated composite structures. In the present displacement field, the nodes along the thickness direction are located at the upper surface and bottom surface and mid-surfaces of each layer. The displacement components are continuous along the thickness direction but the derivatives of the displacements (strains) are discontinuous at the interfaces. Therefore, the displacement field present here is an improvement and extension to the Reddy's theory.

2.2 In-plane displacements discretization

The basic idea of the XLWM is to convert a complex 3D fracture problem to two 2D fracture problem (two 1D fracture problem for composite beams [1]).

For the laminated composite plate with multiple delaminations and transverse cracks, the nodal displacements ($u_{\alpha ik}$) and the addition freedoms ($u_{\alpha lk}$, $u_{\alpha rk}$) are expressed over each element as a linear combination of the Lagrange interpolation, the discontinuous enrichment and the crack-tip enrichment functions as

$$u_{\alpha\zeta k}(x,y,t) = \psi_m(x,y)\tilde{U}_{\alpha\zeta km}(t) + \Lambda_s(x,y)\bar{U}_{\alpha\zeta ks}(t) + \Pi_{h_b}(x,y)\hat{U}_{\alpha\zeta kh_b}(t) \tag{5}$$

where $m = 1, \cdots, N_E$: and N_E is the number of the in-plane finite element nodes; $s = 1, \cdots, N_E^P$, and N_E^P is the number of in-plane nodes which are enriched by the discontinuity of in-plane transverse cracks; $h_b = 1, \cdots, N_E^Q$; and N_E^Q is the number of in-plane nodes which are enriched by the in-plane transverse crack tips; $b = 1, \cdots, N^F$; and N^F is the number of the crack-tip enrichment functions; $\tilde{U}_{\alpha\zeta km}$ is the freedoms of the standard nodes; $\bar{U}_{\alpha\zeta ks}$ is the addition freedoms introduced by the transverse cracks; and $\hat{U}_{\alpha\zeta kh_b}$ is the addition freedoms introduced by the transverse crack tips; $\psi_m(x,y)$ is the two-dimensional Lagrange interpolation function; $\Lambda_s = \psi_s(x,y)F_s^H(x,y)$ is the shape function used to model in-plane cracks and $F_s^H(x,y)$ is the Heaviside function; $\Pi_{h_b} = \psi_h(x,y)F_{h_b}(x,y)$ is the shape function used to model transverse crack tips and the enrichment function $F_{h_b}(x,y)$ will be introduced in Section 2.4.

Because of the nodes along the thickness direction are located at the mid-surface of each ply, the tip of mathematic transverse crack is located at the mid-surface, instead of the interface, as shown in our previous investigations [1]. To truly simulate the tip of real crack, we had presented a scheme based on the concept of sublaminates.

For the laminated composite plate without transverse cracks, the nodal displacements and the addition freedoms in the XLWM can be expressed over each element as a linear combination of the Lagrange interpolation function ψ_m as follows

$$u_{\alpha\zeta k}(x,y,t) = \psi_m(x,y)\tilde{U}_{\alpha\zeta km}(t) \tag{6}$$

2.3 Level set representation of cracks

The level set method (LSM) [42,43], which is a numerical technique for tracking the motion of discontinuous interfaces, is employed here to track the interfaces resulted from the transverse cracks. The crack faces are represented by level curve $\psi(\boldsymbol{x},t) = 0$. The crack tips are represented by the intersection of $\psi(\boldsymbol{x},t) = 0$ and $\phi_i(\boldsymbol{x},t) = 0$ where ϕ_i are also level set functions, and each i denotes a different crack tip.

The initial conditions of the level curve ψ can be defined as the signed-distance to the crack face

$$\psi(\boldsymbol{x}, t=0) = \pm \min_{\boldsymbol{x}_\gamma \in \gamma(t)} \|\boldsymbol{x} - \boldsymbol{x}_\gamma\| \tag{7}$$

where $\gamma(t)$ represents the crack face.

Similarly, the the level curve ϕ_i can be constructed by the signed-distance of the line orthogonal to crack at its tips, namely

$$\phi_i(\boldsymbol{x}, t) = (\boldsymbol{x} - \boldsymbol{x}_i) \cdot \hat{\boldsymbol{t}} \tag{8}$$

where $\boldsymbol{x}_i$ is the location of the i-th crack tip. $\hat{\boldsymbol{t}}$ is the unit vector tangent to the crack at its tip.

Therefore, the crack can be represented by multiple level set functions as

$$\{\boldsymbol{x} : \psi(\boldsymbol{x}, t) = 0 \,\text{and}\, \phi_i(\boldsymbol{x}, t) \leq 0\} \tag{9}$$

where the level sets $\psi = 0$ and $\phi_i = 0$ are forced to be orthogonal at their intersection point.

2.4 Enrichment functions

The enrichment function used to model in-plane cracks is constructed by the Heaviside function

$$F^H(\boldsymbol{x}) = \begin{cases} 1, & \psi(\boldsymbol{x}, t) > 0 \\ -1, & \psi(\boldsymbol{x}, t) < 0 \end{cases} \tag{10}$$

All laminae are orthotropic, so the near-tip functions F_{h_b} must span from the displacement fields derived for orthotropic materials. According to Asadpoure and Mohammadi [30,32], F_{h_b} can be taken as [32,31,30,44]

$$\begin{aligned} F_1 &= \sqrt{r}\cos\frac{\theta_1}{2}\sqrt{g_1(\theta)},\ F_2 = \sqrt{r}\cos\frac{\theta_2}{2}\sqrt{g_2(\theta)}, \\ F_3 &= \sqrt{r}\sin\frac{\theta_1}{2}\sqrt{g_1(\theta)},\ F_4 = \sqrt{r}\sin\frac{\theta_2}{2}\sqrt{g_2(\theta)} \end{aligned} \tag{11}$$

where

$$\begin{aligned} g_j(\theta) &= \sqrt{(\cos\theta + s_{jx}\sin\theta)^2 + (s_{jy}\sin\theta)} \\ \theta_j &= \arctan\left(\frac{s_{jy}\sin\theta}{\cos\theta + s_{jx}\sin\theta}\right) \end{aligned}, \ j = 1, 2 \tag{12}$$

s_{jx} and s_{jy} are the real and imaginary components of the roots of the characteristic equation derived by substituting the Airy stress function into the compatibility equation of anisotropic solids free of body force[44].

For the isotropic plates, F_{h_b} should be taken as

$$\begin{aligned} F_1 &= \sqrt{r}\cos\frac{\theta}{2},\ F_2 = \sqrt{r}\sin\theta\cos\frac{\theta}{2}, \\ F_3 &= \sqrt{r}\sin\frac{\theta}{2},\ F_4 = \sqrt{r}\sin\theta\sin\frac{\theta}{2} \end{aligned} \tag{13}$$

3 Hamilton's principle and Euler-Lagrange equations

Substituting the displacements in Eq.(3) into the strain-displacement relationship results in

$$\begin{aligned} \varepsilon_{xx} &= \Phi_{\zeta k} u_{1\zeta k,x} \quad \varepsilon_{xy} = \Phi_{\zeta k} u_{1\zeta k,y} + \Phi_{\zeta k} u_{2\zeta k,x} \\ \varepsilon_{yy} &= \Phi_{\zeta k} u_{2\zeta k,y} \quad \varepsilon_{yz} = \Phi_{\zeta k,z} u_{2\zeta k} + \Phi_{\zeta k} u_{3\zeta k,y} \\ \varepsilon_{zz} &= \Phi_{\zeta k,z} u_{3\zeta k} \quad \varepsilon_{xz} = \Phi_{\zeta k,z} u_{1\zeta k} + \Phi_{\zeta k} u_{3\zeta k,x} \end{aligned} \tag{14}$$

Thus, the virtual strain energy is given by

$$\begin{aligned} \delta U &= \int_\Omega \int_{-H/2}^{H/2} (\sigma_{xx}\delta\varepsilon_{xx} + \sigma_{yy}\delta\varepsilon_{yy} + \sigma_{zz}\delta\varepsilon_{zz} + \sigma_{xy}\delta\varepsilon_{xy} + \sigma_{yz}\delta\varepsilon_{yz} + \sigma_{xz}\delta\varepsilon_{xz})\,\mathrm{d}z\mathrm{d}x\mathrm{d}y \\ &= \int_\Omega (N^x_{\zeta k}\delta u_{1\zeta k,x} + N^{xy}_{\zeta k}\delta u_{1\zeta k,y} + Q^{xz}_{\zeta k}\delta u_{1\zeta k} + N^y_{\zeta k}\delta u_{2\zeta k,y} + N^{xy}_{\zeta k}\delta u_{2\zeta k,x} + \\ &\quad Q^{yz}_{\zeta k}\delta u_{2\zeta k} + N^{yz}_{\zeta k}\delta u_{3\zeta k,y} + N^{xz}_{\zeta k}\delta u_{3\zeta k,x} + Q^{zz}_{\zeta k}\delta u_{3\zeta k})\mathrm{d}x\mathrm{d}y \end{aligned} \tag{15}$$

where the stress resultants are

$$\begin{aligned} \left(N^x_{\zeta k}, N^y_{\zeta k}, N^{xy}_{\zeta k}, N^{yz}_{\zeta k}, N^{xz}_{\zeta k}\right) &= \int_{-H/2}^{H/2} (\sigma_{xx}, \sigma_{yy}, \sigma_{xy}, \sigma_{yz}, \sigma_{xz})\,\Phi_{\zeta k}\mathrm{d}z, \\ \left(Q^{zz}_{\zeta k}, Q^{yz}_{\zeta k}, Q^{xz}_{\zeta k}\right) &= \int_{-H/2}^{H/2} (\sigma_{zz}, \sigma_{yz}, \sigma_{xz})\,\Phi_{\zeta k,z}\mathrm{d}z \end{aligned} \tag{16}$$

The virtual work done by the external forces is given by

$$\begin{aligned} \delta W &= \int_\Omega [q_b(y,t)\delta u_3(y,-\frac{H}{2},t) + q_t(y,t)\delta u_3(y,\frac{H}{2},t)]\mathrm{d}x\mathrm{d}y + \\ &\quad \int_\Gamma \int_{-H/2}^{H/2} (\bar{\sigma}_{nn}\delta u_n + \bar{\sigma}_{ns}\delta u_s + \bar{\sigma}_{nz}\delta u_3)\,\mathrm{d}z\mathrm{d}\Gamma \\ &= \int_\Omega \left(q_b\delta u_3^{N+2} + q_t\delta u_3^1\right)\mathrm{d}x\mathrm{d}y + \int_\Gamma \left(\bar{N}^{nn}_{\zeta k}\delta u^n_{1\zeta k} + \bar{N}^{ns}_{\zeta k}\delta u^s_{1\zeta k} + \bar{Q}^n_{\zeta k}\delta u_{3\zeta k}\right)\mathrm{d}\Gamma \end{aligned} \tag{17}$$

where q_b and q_t are the distributed force at the bottom surface ($z = -H/2$) and top surface ($z = H/2$) of the laminated plate, respectively; H is the thickness of the composite laminated plates. $\bar{\sigma}_{nn}$, $\bar{\sigma}_{ns}$ and $\bar{\sigma}_{nz}$ are the stresses at the

boundary Γ. Moreover,

$$\begin{aligned}\bar{N}_{\zeta k}^{nn} &= \int_{-H/2}^{H/2} \bar{\sigma}_{nn}\phi_{\zeta k}\mathrm{d}z,\\ \bar{N}_{\zeta k}^{ns} &= \int_{-H/2}^{H/2} \bar{\sigma}_{ns}\phi_{\zeta k}\mathrm{d}z,\\ \bar{Q}_{\zeta k}^{n} &= \int_{-H/2}^{H/2} \bar{\sigma}_{nz}\phi_{\zeta k}\mathrm{d}z\end{aligned} \tag{18}$$

are the boundary stress resultants and

$$\begin{aligned}u_{1\zeta k}^{n} &= u_{1\zeta k}n_x + u_{2\zeta k}n_y\\ u_{1\zeta k}^{s} &= -u_{1\zeta k}n_y + u_{2\zeta k}n_x\end{aligned} \tag{19}$$

are the normal and tangential displacements at boundary.

The virtual kinetic energy is given by

$$\begin{aligned}\delta M &= \int_{\Omega}\int_{-H/2}^{H/2} \rho_0\left(\dot{u}_1\delta\dot{u}_1 + \dot{u}_2\delta\dot{u}_2 + \dot{u}_3\delta\dot{u}_3\right)\mathrm{d}z\mathrm{d}x\mathrm{d}y\\ &= \int_{\Omega}\left(I_{\zeta\eta ke}\dot{u}_{1\eta e}\delta\dot{u}_{1\zeta k} + I_{\zeta\eta ke}\dot{u}_{2\eta e}\delta\dot{u}_{2\zeta k} + I_{\zeta\eta ke}\dot{u}_{3\eta e}\delta\dot{u}_{3\zeta k}\right)\mathrm{d}x\mathrm{d}y\end{aligned} \tag{20}$$

where

$$I_{\zeta\eta ke} = \int_{-H/2}^{H/2} \rho_0\Phi_{\zeta k}\Phi_{\eta e}\mathrm{d}z \tag{21}$$

Substituting Eq.(15), (17) and (20) into the Hamilton's principle

$$\int_0^T (\delta U - \delta W - \delta M)dt = 0 \tag{22}$$

and integrating by parts lead to the following Euler-Lagrange equations

$$\begin{aligned}\delta u_{1\zeta k} :& N_{\zeta k,x}^{x} + N_{\zeta k,y}^{xy} - Q_{\zeta k}^{xz} = I_{\zeta\eta ke}\ddot{u}_{1\eta e}\\ \delta u_{2\zeta k} :& N_{\zeta k,y}^{y} + N_{\zeta k,x}^{xy} - Q_{\zeta k}^{yz} = I_{\zeta\eta ke}\ddot{u}_{2\eta e}\\ \delta u_{3\zeta k} :& N_{\zeta k,y}^{yz} + N_{\zeta k,x}^{xz} - Q_{\zeta k}^{zz} + q_b\delta_k^{N+2} + q_t\delta_k^{1} = I_{\zeta\eta ke}\ddot{u}_{3\eta e}\end{aligned} \tag{23}$$

with the natural boundary conditions

$$\begin{aligned}\delta u_{1\zeta k} :&\ N_{\zeta k}^{nn} - \tilde{N}_{\zeta k}^{nn} = 0\\ \delta u_{2\zeta k} :&\ N_{\zeta k}^{ns} - \tilde{N}_{\zeta k}^{ns} = 0\\ \delta u_{3\zeta k} :&\ Q_{\zeta k}^{n} - \bar{Q}_{\zeta k}^{n} = 0\end{aligned} \tag{24}$$

In Eq.(23), δ_k^0 and δ_k^{N+1} are the Kronecker delta and

$$\begin{aligned}
N_{\zeta k}^{nn} &= N_{\zeta k}^{x} n_x + N_{\zeta k}^{xy} n_y \\
N_{\zeta k}^{ns} &= N_{\zeta k}^{y} n_y + N_{\zeta k}^{xy} n_x \\
Q_{\zeta k}^{n} &= N_{\zeta k}^{yz} n_y + N_{\zeta k}^{xz} n_x \\
\tilde{N}_{\zeta k}^{nn} &= \bar{N}_{\zeta k}^{nn} n_x - \bar{N}_{\zeta k}^{ns} n_y \\
\tilde{N}_{\zeta k}^{ns} &= \bar{N}_{\zeta k}^{nn} n_y + \bar{N}_{\zeta k}^{ns} n_x
\end{aligned} \tag{25}$$

4 Constitutive equations

The constitutive law of the μ-th layer in the composite laminate with respect to the global x-y-z coordinate system is

$$\begin{Bmatrix} \sigma_{xx} \\ \sigma_{yy} \\ \sigma_{zz} \\ \sigma_{yz} \\ \sigma_{xz} \\ \sigma_{xy} \end{Bmatrix}^{(\mu)} = \begin{bmatrix} C_{11} & C_{12} & C_{13} & 0 & 0 & C_{16} \\ C_{12} & C_{22} & C_{23} & 0 & 0 & C_{26} \\ C_{13} & C_{23} & C_{33} & 0 & 0 & C_{36} \\ 0 & 0 & 0 & C_{44} & C_{45} & 0 \\ 0 & 0 & 0 & C_{45} & C_{55} & 0 \\ C_{16} & C_{26} & C_{36} & 0 & 0 & C_{66} \end{bmatrix}^{(\mu)} \begin{Bmatrix} \varepsilon_{xx} \\ \varepsilon_{yy} \\ \varepsilon_{zz} \\ \varepsilon_{yz} \\ \varepsilon_{xz} \\ \varepsilon_{xy} \end{Bmatrix}^{(\mu)} \tag{26}$$

Invoking the constitutive equation in Eq.(26), the force resultants in Eq.(16) can be expressed in terms of the displacements as

$$\begin{aligned}
\left(N_{\zeta k}^{x},\, N_{\zeta k}^{y},\, Q_{\zeta}^{zz},\, N_{\zeta k}^{xy}\right) = {} & \left(A^1_{11\zeta\eta ke},\, A^1_{12\zeta\eta ke},\, A^3_{13\zeta\eta ke},\, A^1_{16\zeta\eta ke}\right) u_{1\eta e,x} + \\
& \left(A^1_{16\zeta\eta ke},\, A^1_{26\zeta\eta ke},\, A^3_{36\zeta\eta ke},\, A^1_{66\zeta\eta ke}\right) \left(u_{1\eta e,y} + u_{2\eta e,x}\right) + \\
& \left(A^1_{12\zeta\eta ke},\, A^1_{22\zeta\eta ke},\, A^3_{23\zeta\eta ke},\, A^1_{26\zeta\eta ke}\right) u_{2\eta e,y} + \\
& \left(A^2_{13\zeta\eta ke},\, A^2_{23\zeta\eta ke},\, A^4_{33\zeta\eta ke},\, A^2_{36\zeta\eta ke}\right) u_{3\eta e} \\
\left(N_{\zeta k}^{yz},\, Q_{\zeta k}^{yz},\, N_{\zeta k}^{xz},\, Q_{\zeta k}^{xz}\right) = {} & \left(A^2_{45\zeta\eta ke}, A^4_{45\zeta\eta ke}, A^2_{55\zeta\eta ke}, A^4_{55\zeta\eta ke}\right) u_{1\eta e} + \\
& \left(A^2_{44\zeta\eta ke}, A^4_{44\zeta\eta ke}, A^2_{45\zeta\eta ke}, A^4_{45\zeta\eta ke}\right) u_{2\eta e} + \\
& \left(A^1_{45\zeta\eta ke}, A^3_{45\zeta\eta ke}, A^1_{55\zeta\eta ke}, A^3_{55\zeta\eta ke}\right) u_{3\eta e,x} + \\
& \left(A^1_{44\zeta\eta ke}, A^3_{44\zeta\eta ke}, A^1_{45\zeta\eta ke}, A^3_{45\zeta\eta ke}\right) u_{3\eta e,y}
\end{aligned} \tag{27}$$

where the laminate stiffness coefficients $A^1_{pq\zeta\eta ke}$, $A^2_{pq\zeta\eta ke}$, $A^3_{pq\zeta\eta ke}$, $A^4_{pq\zeta\eta ke}$ are given in terms of modified elastic constants and the through-thickness

interpolation polynomials as

$$
\begin{aligned}
A^1_{pq\zeta\eta ke} &= \int_{-H/2}^{H/2} \Phi_{\zeta k} C^{(\mu)}_{pq} \Phi_{\eta e} \mathrm{d}z, \\
A^2_{pq\zeta\eta ke} &= \int_{-H/2}^{H/2} \Phi_{\zeta k,z} C^{(\mu)}_{pq} \Phi_{\eta e} \mathrm{d}z, \\
A^3_{pq\zeta\eta ke} &= \int_{-H/2}^{H/2} \Phi_{\zeta k} C^{(\mu)}_{pq} \Phi_{\eta e,z} \mathrm{d}z, \\
A^4_{pq\zeta\eta ke} &= \int_{-H/2}^{H/2} \Phi_{\zeta k,z} C^{(\mu)}_{pq} \Phi_{\eta e,z} \mathrm{d}z,
\end{aligned}
\tag{28}
$$

5 Finite element formulation

5.1 Finite element formulation for laminated plates with multiple delaminations

Substituting Eq.(6) into Eq.(22), the finite element formulation for the static laminated composite plate with multiple delaminations can be expressed as

$$
K_{\alpha\beta\zeta\eta kemn} U_{\beta\eta en} = F_{\alpha\zeta km} \tag{29}
$$

where $m, n = 1, \cdots, N_E$; The contraction of tensor is used inhere, for example, the index pairs α, β in matrix $\boldsymbol{K}$ contract with the index β, so the index α

remain of vector $\boldsymbol{F}$; $K_{\alpha\beta\zeta\eta kemn}$ is the element stiffness matrix given by

$$
\begin{aligned}
K_{11\zeta\eta kemn} =& \psi_{m,x}A^1_{11\zeta\eta ke}\psi_{n,x} + \psi_{m,x}A^1_{16\zeta\eta ke}\psi_{n,y} + \psi_{m,y}A^1_{16\zeta\eta ke}\psi_{n,x} + \\
& \psi_{m,y}A^1_{66\zeta\eta ke}\psi_{n,y} + \psi_m A^4_{55\zeta\eta ke}\psi_n \\
K_{12\zeta\eta kemn} =& \psi_{m,x}A^1_{12\zeta\eta kc}\psi_{n,y} + \psi_{m,x}A^1_{16\zeta\eta kc}\psi_{n,x} + \psi_{m,y}A^1_{26\zeta\eta kc}\psi_{n,y} + \\
& \psi_{m,y}A^1_{66\zeta\eta ke}\psi_{n,x} + \psi_m A^4_{45\zeta\eta ke}\psi_n + \\
K_{13\zeta\eta kemn} =& \psi_{m,x}A^2_{13\zeta\eta ke}\psi_n + \psi_{m,y}A^2_{36\zeta\eta ke}\psi_n + \psi_m A^3_{45\zeta\eta ke}\psi_{n,y} + \psi_m A^3_{55\zeta\eta ke}\psi_{n,x} \\
K_{21\zeta\eta kemn} =& \psi_{m,y}A^1_{12\zeta\eta ke}\psi_{n,x} + \psi_{m,x}A^1_{16\zeta\eta ke}\psi_{n,x} + \psi_{m,y}A^1_{26\zeta\eta ke}\psi_{n,y} + \\
& \psi_{m,x}A^1_{66\zeta\eta ke}\psi_{n,y} + \psi_m A^4_{45\zeta\eta ke}\psi_n = K_{12\zeta\eta kemn} \\
K_{22\zeta\eta kemn} =& \psi_{m,y}A^1_{22\zeta\eta ke}\psi_{n,y} + \psi_{m,y}A^1_{26\zeta\eta ke}\psi_{n,x} + \psi_{m,x}A^1_{26\zeta\eta ke}\psi_{n,y} + \\
& \psi_{m,x}A^1_{66\zeta\eta ke}\psi_{n,x} + \psi_m A^4_{44\zeta\eta ke}\psi_n \\
K_{23\zeta\eta kemn} =& \psi_{m,y}A^2_{23\zeta\eta kc}\psi_n + \psi_{m,x}A^2_{36\zeta\eta kc}\psi_n + \psi_m A^3_{45\zeta\eta kc}\psi_{n,x} + \psi_m A^3_{44\zeta\eta kc}\psi_{n,y} \\
K_{31\zeta\eta kemn} =& \psi_m A^3_{13\zeta\eta ke}\psi_{n,x} + \psi_m A^3_{36\zeta\eta ke}\psi_{n,y} + \psi_{m,y}A^2_{45\zeta\eta ke}\psi_n + \psi_{m,x}A^2_{55\zeta\eta ke}\psi_n \\
=& K_{13\zeta\eta kemn} \\
K_{32\zeta\eta kemn} =& \psi_m A^3_{23\zeta\eta ke}\psi_{n,y} + \psi_m A^3_{36\zeta\eta kc}\psi_{n,x} + \psi_{m,y}A^2_{44\zeta\eta kc}\psi_n + \psi_{m,x}A^2_{45\zeta\eta kc}\psi_n \\
=& K_{23\zeta\eta kemn} \\
K_{33\zeta\eta kemn} =& \psi_{m,y}A^1_{44\zeta\eta ke}\psi_{n,y} + \psi_{m,y}A^1_{45\zeta\eta ke}\psi_{n,x} + \\
& \psi_{m,x}A^1_{45\zeta\eta ke}\psi_{n,y} + \psi_{m,x}A^1_{55\zeta\eta ke}\psi_{n,x} + \psi_m A^4_{33\zeta\eta ke}\psi_n
\end{aligned}
\tag{30}
$$

5.2 Finite element formulation for laminated plates with multiple delaminations and transverse cracks

The finite element formulation for the static laminated composite plate with multiple delaminations and matrix cracks is obtained by substituting Eq.(5) into Eq.(22), as

$$K_{\alpha\beta\zeta\eta ke\kappa\iota}U_{\beta\eta e\iota} = F_{\alpha\zeta k\kappa} \tag{31}$$

where $\kappa = m, s, h_b$; $\iota = n, g, f_b$; $m, n = 1.2, \cdots, N_E$; $s, g = 1, \cdots, N_E^P$; $h_b, f_b = 1, \cdots, N_E^Q$; $b = 1, 2, 3, 4$. The submatrices in Eq.(31) have the same form with the element stiffness matrix of the XLWM for the laminated composite plates Eq.(29). In Eq.(31), the index pairs (m, n), (s, g) and (h_b, f_b) correspond to the shape functions ψ, Λ and $\boldsymbol{\Pi}$, respectively. So, the entries

of $K_{\alpha\beta\zeta\eta ke\kappa\iota}$ can be obtained by replacing the shape functions ψ in Eq.(30) with the shape functions corresponding to the index pairs (m,n), (s,g) and (h_b,f_b), for example

$$\begin{aligned} K_{11\zeta\eta kemg} &= \psi_{m,x}A^1_{11\zeta\eta ke}\Lambda_{g,x} + \psi_{m,x}A^1_{16\zeta\eta ke}\Lambda_{g,y} + \psi_{m,y}A_{16\zeta\eta ke}\Lambda_{g,x} \\ &\quad +\psi_{m,y}A^1_{66\zeta\eta ke}\Lambda_{g,y} + \psi_m A^4_{55\zeta\eta ke}\Lambda_g \\ K_{11\zeta\eta kemf_b} &= \psi_{m,x}A^1_{11\zeta\eta ke}\Pi_{f_b,x} + \psi_{m,x}A^1_{16\zeta\eta ke}\Pi_{f_b,y} + \psi_{m,y}A_{16\zeta\eta ke}\Pi_{f_b,x} \\ &\quad +\psi_{m,y}A^1_{66\zeta\eta ke}\Pi_{f_b,y} + \psi_m A^4_{55\zeta\eta ke}\Pi_{f_b} \end{aligned} \tag{32}$$

For the laminated composite plate with multiple delaminations and transverse cracks, it can be seen from Eqs.(31) that the element stiffness matrix is composed of nine submatrixes. $K_{\alpha\beta\zeta\eta kemn}$ is the submatrix of the nodal freedoms whilst $K_{\alpha\beta\zeta\eta kesg}$ and $K_{\alpha\beta\zeta\eta keh_bf_b}$ are the submatrices of the additional nodal freedoms for delaminations and transverse cracks, respectively. On the other hand, $K_{\alpha\beta\zeta\eta kemg}$, $K_{\alpha\beta\zeta\eta kemf_b}$ and $K_{\alpha\beta\zeta\eta kesf_b}$ are the coupling submatrixes.

6 SIF calculation and crack propagation criterion of the isotropic and orthotropic plates

6.1 SIF calculation

SIF is one of the most important parameters characterizing the crack tip stress field. In XFEM, SIF is usually computed by using the interaction integral method. Kim and Paulino[45] presented a domain integral method for the mix SIF of orthotropic materials. The method has been applied to the SIF calculation of composite structures in many researches [30,32,46–48,34]. In the present work, the method is employed to calculate the SIFs associated with the delaminations and transverse cracks, The method is introduced briefly as follows.

The interaction integral method is carried out by using actual and auxiliary displacement/stress/strain fields. The actual field describes the physical problem and satisfies the equilibrium and compatibility equations in each point of a general inhomogeneous domain. In contrast, auxiliary fields do not satisfy all governing equations (e.g. equilibrium, compatibility and constitutive equations) and are employed to established the relationship between mix SIF and the interaction integral.

For the isotropic materials, the SIF K_{I} and K_{II} are related to the J-integral M_1 of the auxiliary field as

$$M^l = \frac{2}{E^*}\left(K_{\mathrm{I}}^{\mathrm{aux}}K_{\mathrm{I}} + K_{\mathrm{II}}^{\mathrm{aux}}K_{\mathrm{II}}\right) \tag{33}$$

where $K_{\mathrm{I}}^{\mathrm{aux}}$ and $K_{\mathrm{II}}^{\mathrm{aux}}$ are the SIF of the auxiliary field. Detailed expression of M^l can be found in reference [44].

$$E^* = \begin{cases} E & \text{plane stress} \\ \dfrac{E}{1-v^2} & \text{plane strain} \end{cases}$$

E is the elastic modulus of isotropic materials.

For the anisotropic materials, one can obtain the modes I and II SIF K_{I} and K_{II} by solving the linear algebraic equations

$$\begin{cases} M_1^l = 2c_{11}K_{\mathrm{I}} + c_{12}K_{\mathrm{II}} & (K_{\mathrm{I}}^{\mathrm{aux}} = 1, K_{\mathrm{II}}^{\mathrm{aux}} = 0) \\ M_2^l = c_{12}K_{\mathrm{I}} + 2c_{22}K_{\mathrm{II}} & (K_{\mathrm{I}}^{\mathrm{aux}} = 0, K_{\mathrm{II}}^{\mathrm{aux}} = 1) \end{cases} \tag{34}$$

where M_1^l and M_2^l denote the J-integral for the case I ($K_{\mathrm{I}}^{\mathrm{aux}} = 1$, $K_{\mathrm{II}}^{\mathrm{aux}} = 0$) and case II ($K_{\mathrm{I}}^{\mathrm{aux}} = 0$, $K_{\mathrm{II}}^{\mathrm{aux}} = 1$). M_1^l, M_2^l, c_{11}, c_{12} and c_{22} can be found in Reference [44].

Thus SIF K_{I}^{μ} and K_{II}^{μ} of each mathematical layer in the XLWM can be calculated.

6.2 Crack propagation criterion

The maximum circumferential tensile stress criterion [49] assumes that a crack starts to propagate when the maximum circumferential SIF exceed the critical SIF at the direction perpendicular to the maximum circumferential stress-direction. For isotropic materials, the propagation criterion is

$$K_{\theta\max} = \frac{K_{\mathrm{I}}}{K_{\mathrm{Ic}}}\cos^3\frac{\theta_0}{2} - \frac{3}{2}\frac{K_{\mathrm{II}}}{K_{\mathrm{Ic}}}\cos\frac{\theta_0}{2}\sin\theta_0 = K_{\theta C} \tag{35}$$

and the propagation direction is given by

$$\begin{aligned} &K_{\mathrm{I}}\sin\theta_0 - K_{\mathrm{II}}\left(3\cos\theta_0 - 1\right) = 0 \\ &K_{\mathrm{I}}\cos\frac{\theta_0}{2}\left(1 - 3\cos\theta_0\right) + K_{\mathrm{II}}\sin\frac{\theta_0}{2}\left(9\cos\theta_0 + 5\right) < 0 \end{aligned} \tag{36}$$

where $K_{\theta C}$ is the fracture toughness.

In 1987, Saouma el at.[50] extended the maximum circumferential tensile stress criterion of isotropic materials to the crack growth problem of anisotropic materials. The crack growth angle, global coordinates and the crack tip coordinates for the anisotropic materials are shown in Figure 3.

For the anisotropic materials, the crack growth angle θ_0 need to meet

$$\frac{\sigma_\theta}{\sigma_{\theta\max}} = \frac{K_{\mathrm{I}}\mathrm{Re}\left[A\left(\mu_1 B_2 - \mu_2 B_1\right)\right] + K_{\mathrm{II}}\mathrm{Re}\left[A\left(B_2 - B_1\right)\right]}{K_{\mathrm{Icr}}^1\cos^2\beta + K_{\mathrm{Icr}}^2\sin^2\beta} = 1 \tag{37}$$

where σ_θ is the circumferential tensile stress; $\sigma_{\theta\max}$ is the maximum circumferential tensile stress; $\beta = \theta_0 + \omega$ and ω is the angle between the crack and

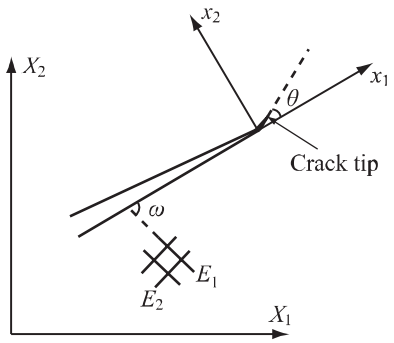

Fig. 3 The crack growth angle, global and local coordinates of the crack tip for the anisotropic materials

the material direction: $A = \dfrac{1}{\mu_1 - \mu_2}$, $B_i = (\cos\theta + \mu_i \sin\theta)^{1.5}$; K^1_{Icr} and K^2_{Icr} are the critical SIF for cracks along direction x_1 and x_2, respectively. The coefficients μ_1 and μ_2 can be found in reference[44].

There are two fronts of the transverse crack in the proposed XLWM: the front in the thickness direction and the front in in-plane. In the proposed study, only the front in in-plane is considered. For the front in the thickness direction, if the virtual crack closure technique (VCCT) is employed to calculate the strain energy release rate (SERR) along the transverse crack front, and the transverse crack growth in the thickness direction can be predicted by the mixed-mode fracture criterion.

7 Local remesh for crack arbitrary growth

As the crack grows, some nodes such as node O in Figure 4 may become very close to the crack surface. When one part of an element divided by a crack is far smaller than another part, Guass integral cannot accurately obtain the stiffness matrix of the element and would result in significant error. Because the level set function cannot be accurately calculated nearby the turning point of a crack, the whole calculation process may be terminated. In order to overcome this problem, a local remesh is undergone near the crack by moving the node O to O', as shown in Figure 4. Let l_{gap} denote the minimum distance between node O and the intersection point of the element edge and the crack. As the crack grows, l_{gap} determines whether one needs to move the node (local remesh). To restrict excess element distortion, the node is moved by

$$\Delta \boldsymbol{x} = f l_e \boldsymbol{n} \tag{38}$$

where l_e is the length of the element edge; f is the coefficient that limits the distance of move and excess element distortion; $\boldsymbol{n}$ is the outward normal vector of crack surface. As an illustration, there are nodes very close to the crack surface in Figure 5(a), After the local remeshing with $f = 0.2$, nodes are

shifted away from the crack surface while the mesh quality is reserved as shown in Figure 5(b). The large value of f would result into the grid distortion and the small value cannot make the nodes away from the crack surface adequately, so the value of $f = 0.2$ is determine by a number of examples.

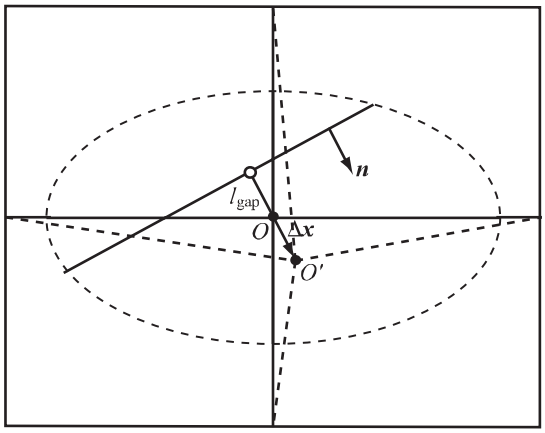

Fig. 4 Scheme of local remesh.

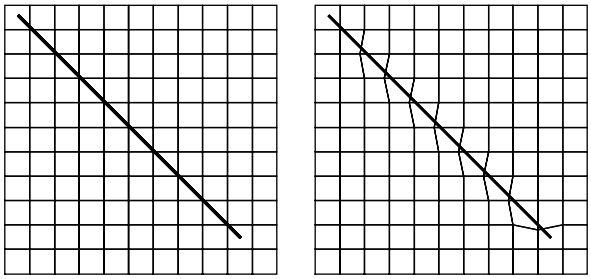

Fig. 5 Local remesh. (a) Before local remesh; (b) After local remesh.

The integration scheme for elements enriched by strong discontinuous function is based on subdomains (sub-triangle), its details can be found in Refs. [44, 51]. In this approach, the enriched elements are to subdivide into sub-triangles at both sides of the crack whose edges are adapted to crack faces. For the crack tip elements, more sub-triangles are required in front of the crack tip because of the existence of a highly nonlinear and singular stress field.

8 Numerical examples

8.1 Static responses analysis

The XLWM is used to model the plates with multiple delaminations and/or transverse crack. Figure 6 shows the geometry and FE mesh for a rectangular plate with a semi-elliptic delamination and a transverse crack. The major axis of the delamination coincides with the y-axes. The transverse crack is along the minor axis of the ellipse. Three kinds of boundary conditions are investigated: 1) $x = 6$ is clamped and other edges are free (CFFF); 2) $y = 10$ and $y = 0$ are clamped and other edges are free (CCFF); 3) $x = 0$ is free and other edge are clamped (CCCF). The plate is subjected to a unit transverse pressure on the delaminated region in top surface.

The plate of overall thickness H=0.4 m is evenly divided into eight layers. For comparison purpose, these problems are also analyzed by using MSC.Nastran with Hex8 solid elements. Nodes pairs along the delamination interface and through-thickness crack are employed to model the displacement discontinuity. Meanwhile, the discretization scheme of the XLWM is the same with that used in the finite element analysis.

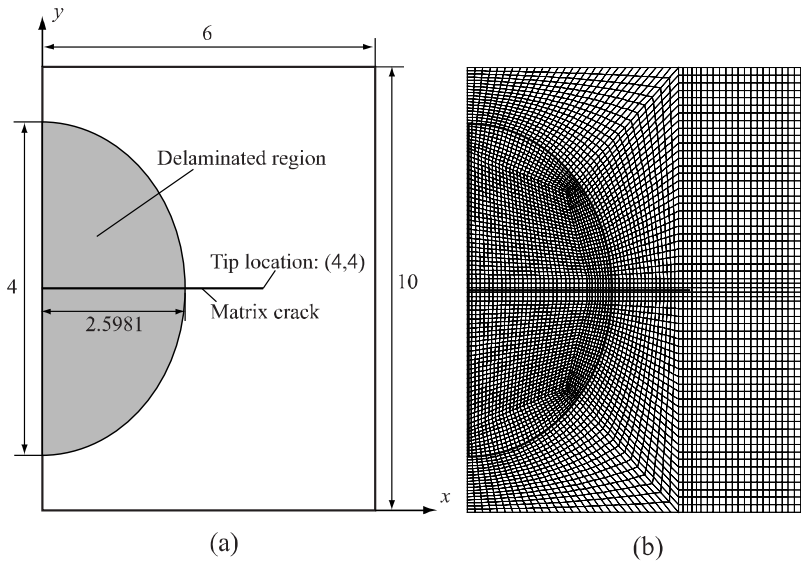

Fig. 6 Composite laminated plate with elliptic delamination and transverse crack. (a) Schematic diagram; (b) FE mesh. (The length dimension is in m.)

Firstly, the isotropic plates with delamination and/or transverse crack are employed to validate the proposed XLWM. The material properties are taken as $E = 52\text{GPa}$, $\nu = 0.3$.

Table 1 and Table 2 compare the maximum displacements obtained by the proposed XLWM and MSC.Nastran for the isotropic plates with delamination or through crack, respectively. In the damage zone, the delamination can be denoted as $[\theta/\theta/\theta/\theta/\cap/\theta/\theta/\theta/\theta]$, which means that the delamination is located at the interface between 4-th layer and 5-th layer (4-th interface). It can be seen from the table that the proposed method is accurate and reliable for the plates with delamination or through crack. In Table 1, the maximum displacements u_1 and u_3 occur at the central point of the delamination region ($x = 0$, $y = 5$), and the maximum displacement u_2 occurs at the point ($x = 0$, $y = 2.8$) and ($x = 0$, $y = 7.2$). In Table 2, the maximum displacement u_1 occurs at the central point of the delamination region ($x = 0$, $y = 5$) for CFFF, point ($x = 2.9$, $y = 5.0$) for CCFF and point ($x = 2.6$, $y = 5.0$) for CCCF. The maximum displacement u_2 occurs at the point ($x = 0$, $y = 0$) and ($x = 0$, $y = 10.0$) for CFFF, point ($x = 0$, $y = 3.4$) and ($x = 0$, $y = 6.6$) for CCFF and CCCF. The maximum displacements u_3 occurs at the central point of the delamination region.

Table 1 Maximum displacement of the isotropic plates with elliptic delamination.

BC	Num. of nodes	u_1 (10^{-5}m)		u_2 (10^{-6}m)		u_3 (10^{-4}m)	
		MSC	XLWM	MSC	XLWM	MSC	XLWM
CFFF	2090		1.35393		3.35562		2.99266
	5140		1.45269		3.30989		3.04532
	6286	1.49643	1.45888	3.44315	3.33837	3.28209	3.20157
CCCF	2090		0.34896		3.26685		0.70077
	5140		0.36917		3.41381		0.72090
	6286	0.38195	0.37177	3.52243	3.44705	0.74457	0.72615
CCFF	2090		0.34402		3.31871		0.70862
	5140		0.36395		3.47041		0.72944
	6286	0.37653	0.36651	3.58173	3.50424	0.75339	0.73473

Table 2 Maximum displacement of the isotropic plates with transverse crack.

BC	Num. of nodes	u_1 (10^{-6}m)		u_2 (10^{-6}m)		u_3 (10^{-5}m)	
		MSC	XLWM	MSC	XLWM	MSC	XLWM
CFFF	2090		12.19856		2.41575		26.85609
	5140		12.86313		2.40270		28.49373
	6286	13.22468	12.90100	2.49105	2.42031	29.3749	28.63100
CCCF	2090		2.04472		2.85328		4.74906
	5140		2.13233		2.96655		4.94175
	6286	2.18307	2.14423	3.02683	2.97985	5.08927	5.00548
CCFF	2090		1.92158		3.11804		5.12707
	5140		1.99643		3.24751		5.34512
	6286	2.03693	2.00772	3.31632	3.26068	5.51124	5.41431

For the isotropic plates with delamination and non-thick-through crack, the maximum displacements calculated by XLWM and MSC.Nastran are compared in Table 3. In the damage region, the delamination and crack can be

denoted as $[\theta/\theta/\theta/\theta/ \cap /\boldsymbol{\theta}/\boldsymbol{\theta}/\boldsymbol{\theta}/\boldsymbol{\theta}]$, which means that the delamination is located at the interface between 4-th layer and 5-th layer and the crack cuts though the last four layers. It can be seen from Table 3 that the proposed method is accurate and reliable for the isotropic plates with both delamination and crack. The locations of maximum displacements are same with those in Table 2.

Table 3 Maximum displacement of the isotropic plates with delamination and transverse crack.

BC	u_1 (10^{-6}m)		u_2 (10^{-6}m)		u_3 (10^{-4}m)	
	MSC	XLWM	MSC	XLWM	MSC	XLWM
CFFF	14.58864	14.24940	5.42915	5.25124	3.51073	3.42605
CCCF	4.35420	4.28484	4.46578	4.37015	1.04054	1.02144
CCFF	4.20282	4.14198	4.65572	4.54863	1.06545	1.04501

The XLWM is also employed to model the cross-ply laminated plate with multiple delaminations and/or transverse cracks in this example. The material properties of the single layer are taken as $E_{11} = 181\text{GPa}$, $E_{22} = E_{33} = 10.3\text{GPa}$, $G_{12} = G_{13} = 7.17\text{GPa}$, $G_{23} = 6.21\text{GPa}$, $\nu_{12} = 0.28$, $\nu_{13} = 0.02$, and $\nu_{23} = 0.40$.

For the three stacking sequences $[0]_8$, $[0/90/0/90]_s$ and $[90/0/90/0]_s$, Table 4 compares the maximum displacements calculated by XLWM and MSC.Nastran for the plates with delamination $[\theta/\theta/\theta/\theta/ \cap /\theta/\theta/\theta/\theta]$. It can be seen from Table 4 that the proposed method is also accurate and reliable for the plates with transverse crack.

Table 4 Maximum displacement of the laminated composite plates with transverse crack.

	BC	u_1 (10^{-6}m)		u_2 (10^{-5}m)		u_3 (10^{-4}m)	
		MSC	XLWM	MSC	XLWM	MSC	XLWM
$[0]_8$	CFFF	5.01844	4.99346	0.38525	0.38156	1.19114	1.18586
	CCCF	3.88164	3.84104	0.57331	0.56740	0.96525	0.95664
	CCFF	6.15848	6.06648	1.32531	1.29033	2.21315	2.15968
$[0/90/0/90]_s$	CFFF	6.75187	6.71632	0.38373	0.38006	1.58868	1.58058
	CCCF	2.45285	2.43959	0.34860	0.34687	0.59886	0.59565
	CCFF	2.75320	2.73721	0.42823	0.42560	0.72470	0.72024
$[90/0/90/0]_s$	CFFF	12.33980	12.24270	4.35336	4.28203	2.84058	2.81729
	CCCF	1.82850	1.82283	2.42813	2.41897	0.42132	0.41972
	CCFF	1.83708	1.83281	2.53723	2.52786	0.43750	0.43596

For the laminated composite plate $[0/90/0/90]_s$ with multiple delaminations and transverse cracks, the boundary condition is CCCF. In the damage region, the delaminations and non-thick-though transverse cracks can be denoted as $[\boldsymbol{\theta}/\boldsymbol{\theta}/ \cap /\theta/\theta/\theta/\theta/ \cap /\boldsymbol{\theta}/\boldsymbol{\theta}]$ which means that delaminations are located at the 2-th and 6-th interfaces and the cracks cut though the first two and the last two layers. Deformations and stresses of the laminated composite

plate with multiple elliptic delaminations and transverse cracks are plotted in Figures 7 and 8.

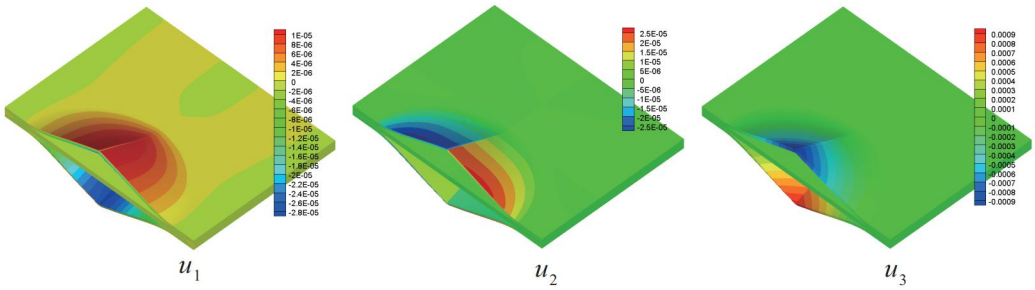

Fig. 7 Deformation of the composite laminated plate with multiple elliptic delaminations and transverse crack.

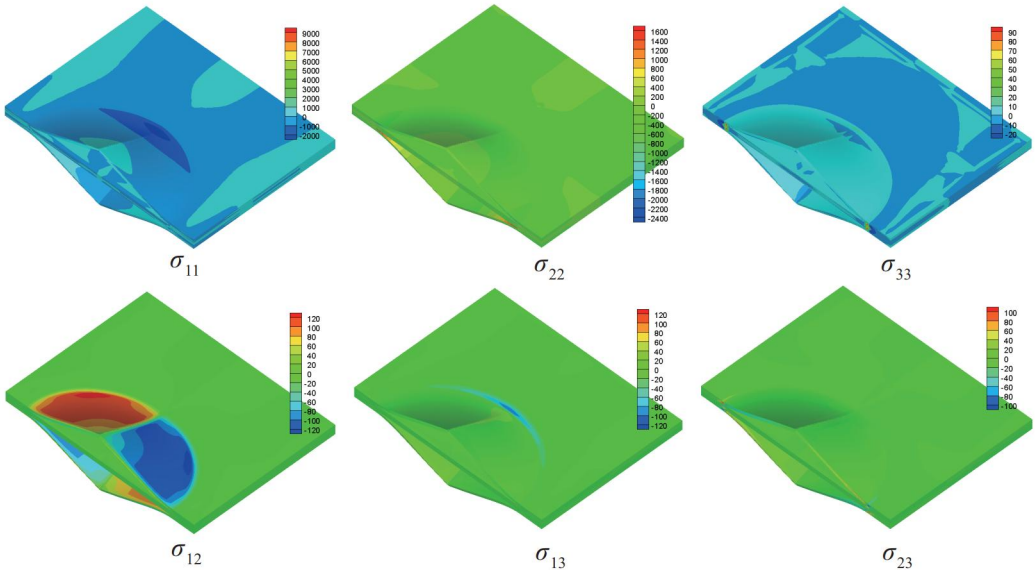

Fig. 8 Stresses of the composite laminated plate with multiple elliptic delaminations and transverse crack.

8.2 SIF calculation

The rectangular isotropic and composite plates with an edge through crack are used to examine the performance of the present method for the SIF calculation. The results obtained by the present method are compared with those given by

the analytical solutions and the available numerical results. In addition, the effects of the crack size and the orthotropic angle on the distribution of SIF along the thickness direction are investigated.

8.2.1 Rectangular isotropic plates with a through-thickness edge crack

The rectangular isotropic plate with a through-thickness crack (see Figure 9(a)) is employed to validate the present method for the calculation of SIF. As shown in Figure 9(a), the plate is subjected to a unit tensile stress σ_0 at two ends and the crack angle φ is the angle between the crack and the direction transverse to the tensile stress. The square region around the crack tip is the domain used for computing the J-integral. The length of the rectangular plate is twice the width. The material parameters are $E = 1.0$ GPa, and $\nu = 0.3$. Two different meshes shown in Figure 9(b) and (c) are used. When the crack angle $\varphi = 0$, SIF $K_{II} = 0$ and the analytical solution of K_{I} is given by

$$K_{\mathrm{I}} = \left[1.12 - 0.23\left(\frac{a}{b}\right) + 10.56\left(\frac{a}{b}\right)^2 - 21.74\left(\frac{a}{b}\right)^3 + 30.42\left(\frac{a}{b}\right)^4\right]\sigma_0\sqrt{\pi a} \tag{39}$$

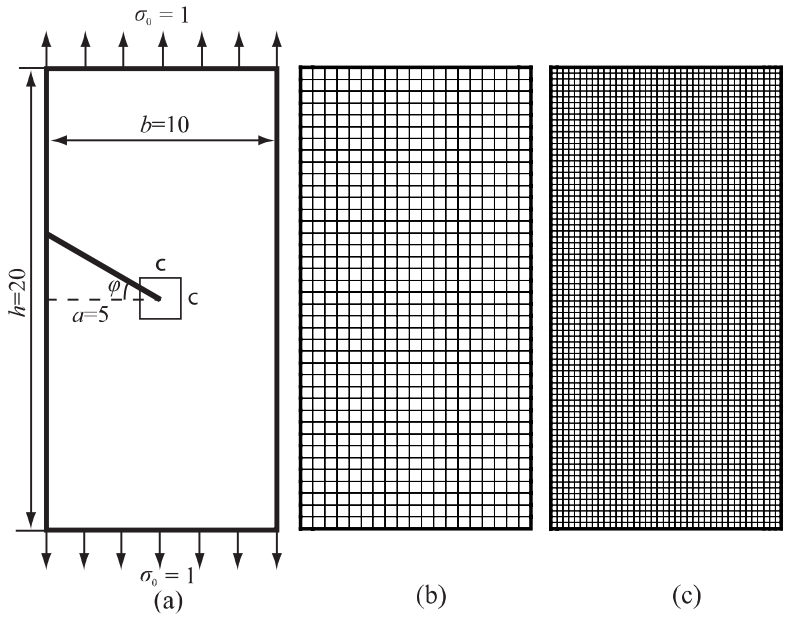

Fig. 9 Rectangular isotropic plates with an edge through crack. (a) Geometric size and crack size; (b) 20×40 elements; (c) 40×80 elements

For different crack lengths, the values of K_{I} of the rectangular isotropic plates with an edge through crack calculated by the present method, Moham-

madi [44] and the analytical method are compared in Table 5. The present predictions agree well with those of the others.

Table 5 K_{I} of the rectangular isotropic plates with an edge through crack.

a/b	Analytical	20×40		40×80		50×100	70×140	80×160
		Ref.[44]	XLWM	Ref.[44]	XLWM	XLWM	XLWM	XLWM
0.30	1.660	1.630	1.478	1.646	1.586	1.608	1.633	1.650
0.45	2.420	2.362	2.155	2.396	2.325	2.437	2.451	2.465
0.60	4.027	3.876	3.549	3.961	3.828	3.884	3.951	3.992

Because the XLWM is quasi three dimensional and the transverse cracks of each single layer are independently described, the distribution of the SIF along the thickness direction can be obtained by the present method. It is an important advantage compared with the existing shell elements enriched by XFEM. For different crack sizes, distributions of K_{I} of the rectangular isotropic plates with an edge through crack are plotted in Figure 10, which shows that the crack size has significant influence on the distribution of K_{I} along the thickness direction. In general, the SIF at top and bottom surfaces is larger than that at the mid-plane. If the ratio of crack size to the width of plate is approaches 0.5, K_{I} decreases from the surface to the mid-plane. If the ratio of crack size to the width of plate is greater or less than 0.5, K_{I} first decreases and then increases from the top/bottom surfaces to mid-plane. Because the boundary condition and the loads are symmetrical with respect to the mid-plane in the present numerical example, the distribution of K_{I} along the thickness direction is symmetrical as well.

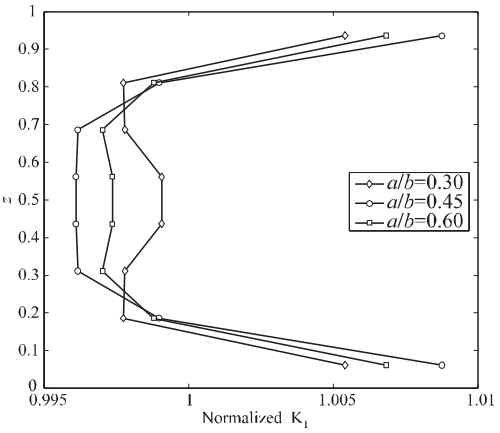

Fig. 10 Distribution of K_{I} of the rectangular isotropic plates with an edge through crack.

The influence of the angle between the crack and the transverse direction of plate φ on SIF is investigated in this numerical example and plotted in

Figure 11, where the values of SIF is the average along the thickness direction. It can be seen that K_{I} decreases as angle φ increases, while K_{II} first increases and then decreases with turning point at $\varphi \approx 30°$.

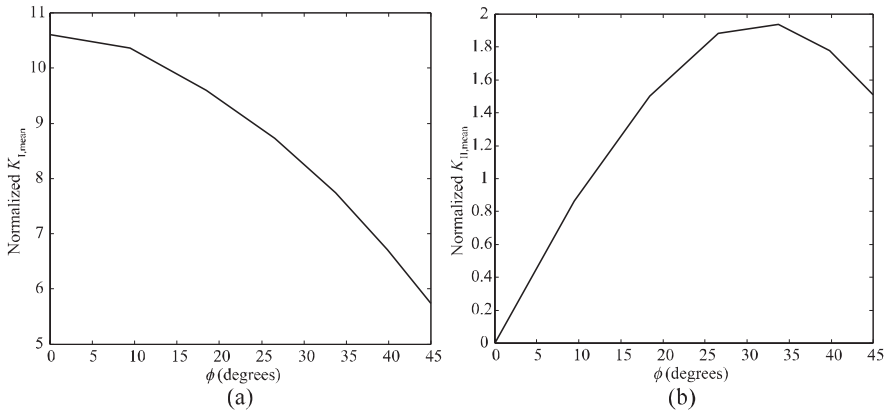

Fig. 11 Influence of angle ϕ on SIF.

For different angles φ, distributions of SIF K_{I} and K_{II} along the thickness direction after normalized by their respective thickness averages are shown in Figure 12. As angle φ increases, the change in amplitude of K_{I} along the thickness direction first decreases and then increases. If angle $\varphi \approx 18°$, K_{I} does not change along the thickness direction. If angle φ is less than 18°, K_{I} decreases from the top/bottom surface to the mid-plane. If angle φ is greater than 18°, K_I increases from the top/bottom surface and attains it maximum at the mid-plane, while K_{I} at the upper/bottm surface is maximum when angle φ is less than 18°. As angle φ increases, the change in amplitude of K_{II} along the thickness direction first decreases and then become almost zero when angle $\varphi \approx 45°$. K_{II} decreases from the top/bottom surface to the mid-plane, namely, K_{II} at top/bottom surface is maximum. K_{I} and K_{II} are symmetrical along the thickness direction with respect to the mid-plane, and always equal to their respective average values at $z/H \approx 0.2$ and $z/H \approx 0.8$.

8.2.2 Rectangular composite plates with an edge through crack

The rectangular composite plate with an edge though crack to be considered has the same geometric size, boundary condition, loads and mesh with the isotropic plate in above subsection. The material properties are $E_{11} = 114.8\,\mathrm{GPa}$, $E_{22} = E_{33} = 11.7\,\mathrm{GPa}$, $G_{12} = G_{13} = 9.66\,\mathrm{GPa}$, $G_{23} = 6.21\,\mathrm{GPa}$, $\nu_{12} = \upsilon_{13} = 0.21$, and $\nu_{23} = 0.40$.

For five fibre angles (0°, 30°, 45°, 60° and 90°), Figure 13 compares the normalized K_{I} and K_{II} obtained by the presented method with those obtained by XFEM [32, 52], BEM [53] and XEFG [54]. The SIF results obtained by the XLWM agree well with those obtained by other methods.

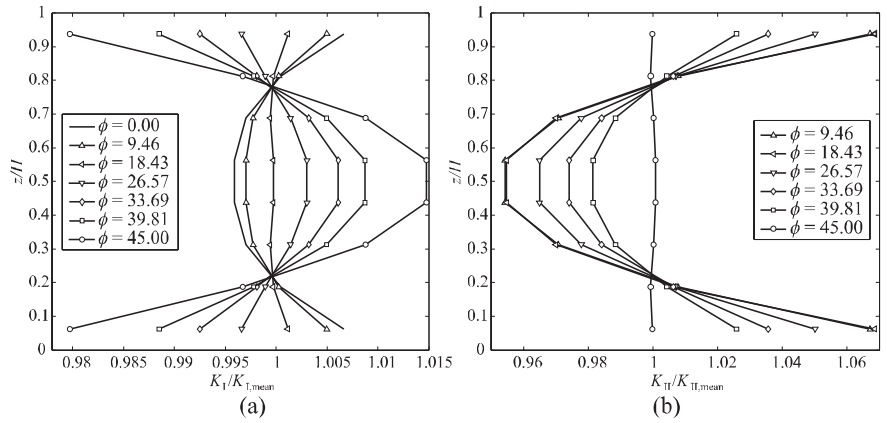

Fig. 12 Distributions of SIF along the thickness direction for different angles ϕ

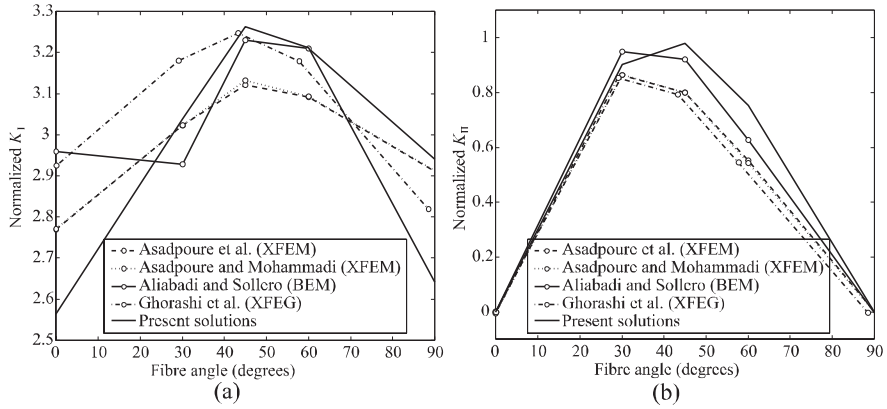

Fig. 13 Comparison of SIF for rectangular composite plates with an edge crack

Figure 14 shows the distributions of SIF along the thickness direction. When fibre angle $\theta = 45°$, the change in amplitude of K_{I} along the thickness direction is maximum. When fibre angle $\theta = 90°$, the change in amplitude is minimum. The change in amplitude of SIF K_{II} along the thickness direction decreases as the fibre angle increasing. Similar to the isotropic plate with an edge crack, K_{I} and K_{II} are symmetrical along the thickness direction with respect to the mid-plane, and K_{I} and K_{II} always equal to their respective average values near the points $z/H \approx 0.2$ and $z/H \approx 0.8$.

The influence of the crack angle φ on SIF for the rectangular composite plate with an edge crack is also examined. Figure 15 shows the influence of φ on SIF for five fibre angles. K_{I} and its change in amplitude decrease as φ increases. On the other hand, the decrease in amplitude of SIF reduces as the fibre angle increasing. K_{II} increases as angle φ increases, and the increase in

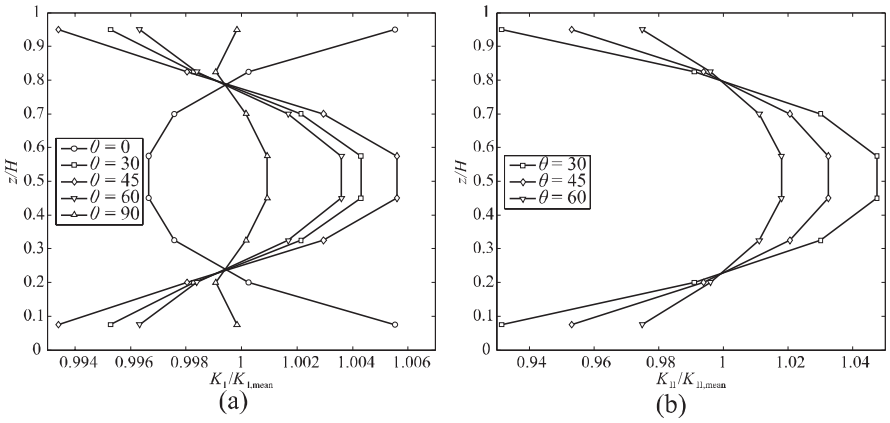

Fig. 14 Distribution of SIF along the thickness direction for the rectangular composite plates with an edge crack

amplitude of K_{II} for $\theta = 0°$ is significantly higher than that for other fibre angles.

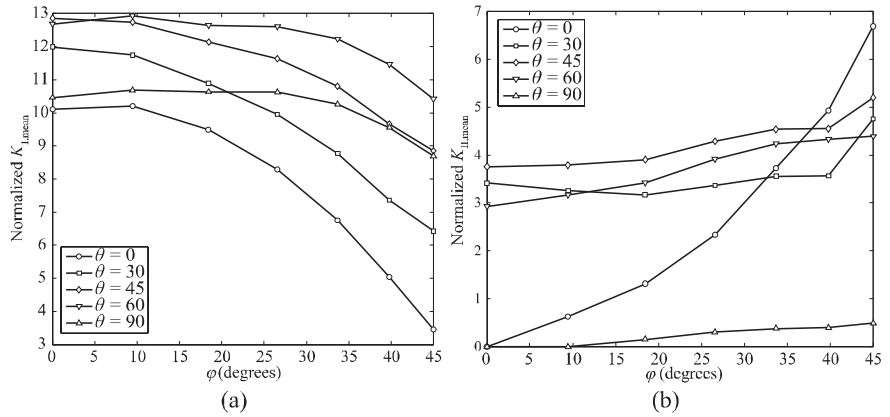

Fig. 15 Influence of angle φ on SIF of the composite plate

Figures 16-20 show the distributions of SIF along the thickness direction for the five fibre angles θ and different crack angles φ. K_{I} and K_{II} are symmetrical along the thickness direction with respect to the mid-plane and always equal to their respective average values near the points $z = 0.2$ and $z = 0.8$. When $\theta = 0°$, the change in amplitude of the SIF K_{I} and K_{II} along the thickness direction first decreases and then increases as φ increases. When angle $\varphi \approx 26°$, the change in amplitude is minimum. When $\theta = 30°, 45°$ and $60°$, the change in amplitude of K_{I} and K_{II} along the thickness direction decreases as the angle φ increases. $\theta = 90°$, the change in amplitude of K_{I} along the thickness direction increases for increasing φ. That of K_{II} is just the opposite.

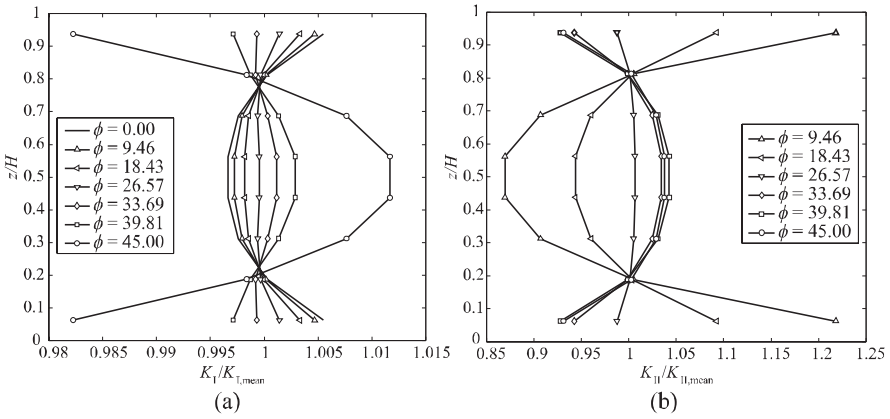

Fig. 16 Distribution of SIF along the thickness direction for the composite plate with an edge crack ($\theta = 0°$)

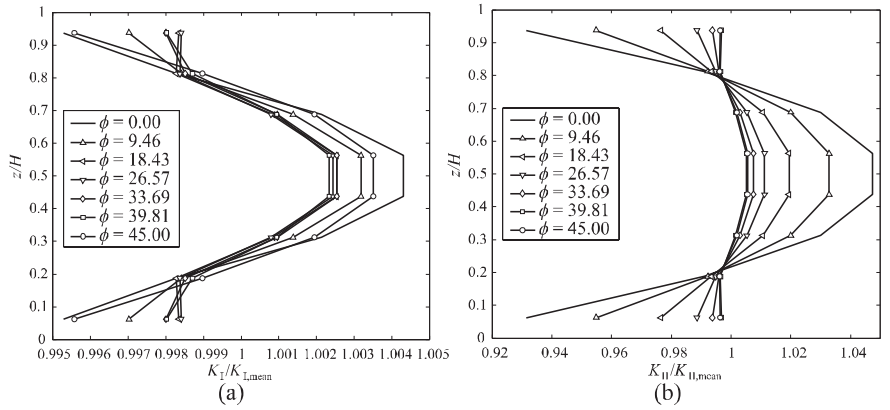

Fig. 17 Distribution of SIF along the thickness direction for the composite plate with an edge crack ($\theta = 30°$)

8.3 Transverse crack arbitrary growth

Crack growth predictions are carried out in this section for plates with an edge through crack and for plates with both an edge through crack and an semi-elliptical delamination. Both isotropic and composite plates are considered. The effects of the fibre angle on the growth angle are investigated.

8.3.1 Rectangular composite plates with edge through cracks

The isotropic plate employed in Section 8.1, see Figure 5, is first considered. The initial crack length is 1.5 m and the crack angle φ is zero. The average crack growth angle is used to update the location of crack tip. Figure 21 shows the effect of the crack size on the K_I. The predicted growth angle is

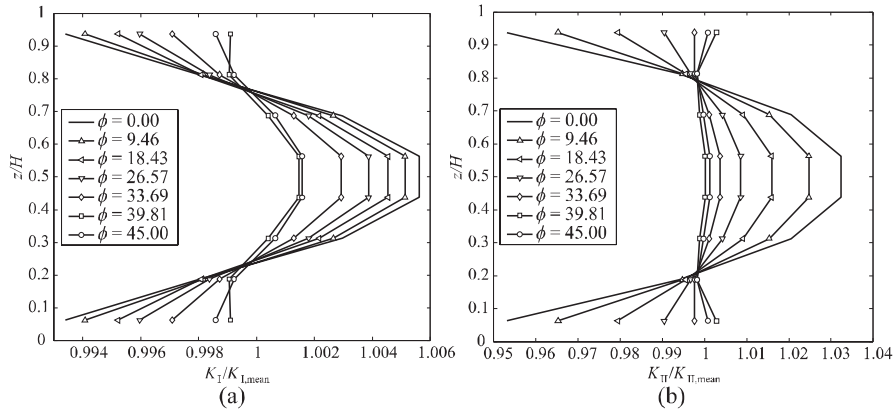

Fig. 18 Distribution of SIF along the thickness direction for the composite plate with an edge crack ($\theta = 45°$)

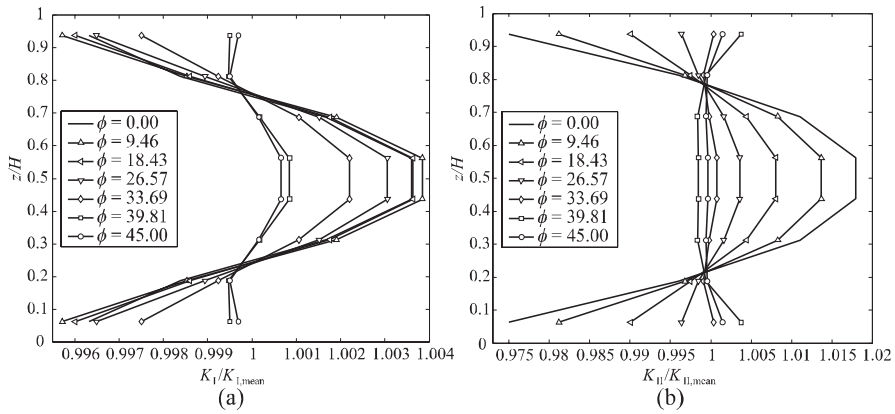

Fig. 19 Distribution of SIF along the thickness direction for the composite plate with an edge crack ($\theta = 60°$)

zero, which agrees with the analytical solution. As the crack grows, K_{I} first increases slowly and then quickly. Moreover, the predicted SIF in all layers are graphically indistinguishable as noted in the figure.

The composite plate employed in Section 8.1, see Figure 6, is then considered. The initial crack length is 3.5 m and the crack angle φ is zero. Again, the average crack growth angle is used to update the location of crack tip. The predicted K_{I} and K_{II} versus the crack size are shown in Figure 22. Figure 23 shows the growth paths for different fibre angle. As the crack grows, K_{I} increases whilst K_{II} first increases and then decreases. If the fibre angle $\theta = 0°$ and 90°, the crack growth angle predicted by the present method is zero. From the existing solution [55], the crack growth angle varies approximately $sin(2\theta)$ with the maximum and minimum growth angles occurring at $\theta = 35^{\circ}$ and $\theta = 135°$, respectively. For the fibre angles considered in this numerical exam-

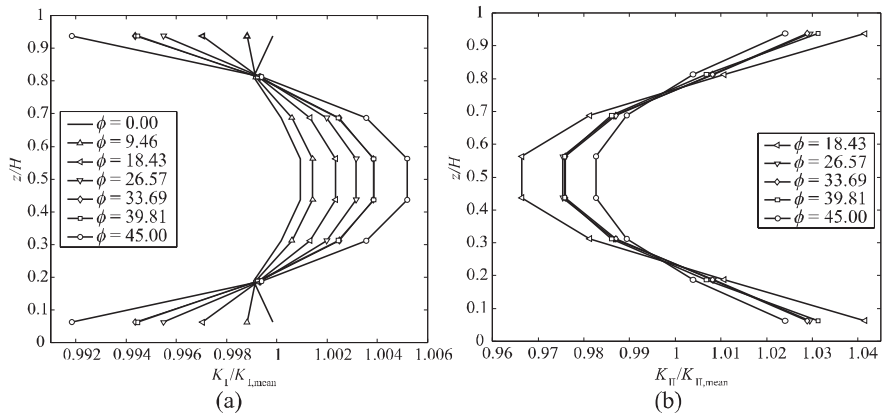

Fig. 20 Distribution of SIF along the thickness direction for the composite plate with an edge crack ($\theta = 90°$)

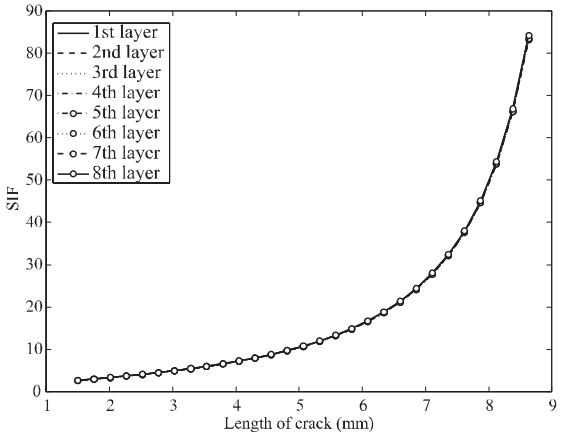

Fig. 21 Effect of the crack size on the SIF for the rectangular isotropic plates with an edge through crack

ple, the maximum value of growth angle occurs when $\theta = 30°$, which somehow agrees with the existing solution.

8.3.2 Rectangular composite plates with semi-elliptical delaminations

SIF and crack growth prediction are conducted for the rectangular composite plate with an elliptic delamination and an edge through crack shown in Figure 6. The initial crack length is 3.02 mm, and the delamination is located at the mid-plane. A unit uniform load is imposed on the top and bottom surfaces of the delaminated region, and a unit tensile stress is applied to the upper and lower edges of the plate.

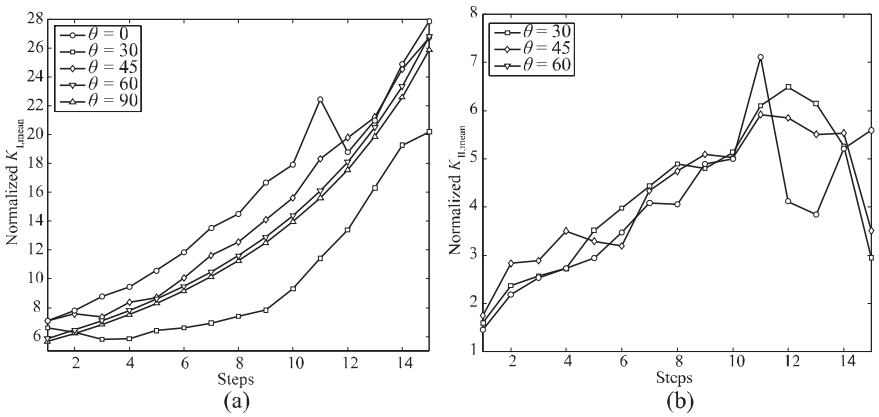

Fig. 22 Variation of SIF versus the crack size in different fibre angle for the rectangular composite plates with an edge crack

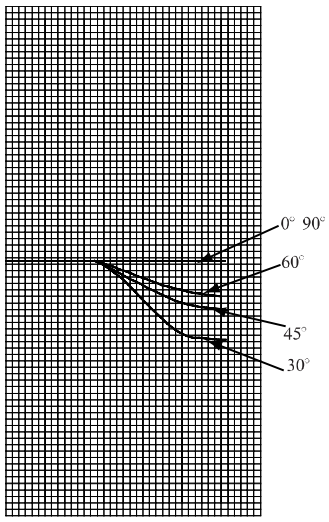

Fig. 23 The crack growth path for different fibre angles

The crack growth problem of the isotropic plate with delamination and crack is first considered. The material properties are $E = 52\text{GPa}$, and $\nu = 0.3$. Figures 24 and 25 portray how the predicted SIF varies with the crack length and along the thickness direction. Figure 24 shows that K_{I} increases as the crack size increases. Figure 24 shows that the SIF assumes its maximum value when the crack tip is very close to the delamination front as in the case of crack length equal to 3.1805 m. Otherwise, the maximum values occurs at the top/bottom surfaces. In other words, the delamination front signicantly affects the crack tip stress field. K_{I} and K_{II} are symmetrical along the thickness direction with respect to the mid-plane. The displacement and stress contours are shown in Figures 26 and 27, respectively. In the crack growing process,

stress concentration appears at the transverse crack tip and delamination front. Stress concentrations of σ_{11} and σ_{22} are most significant along $\omega = 0°$ and $\omega = \pm 90°$ which define the minor and major axis of the semi-elliptical delamination, respectively. Meanwhile, stress concentration of σ_{12} is most significant along $\omega = \pm 45°$.

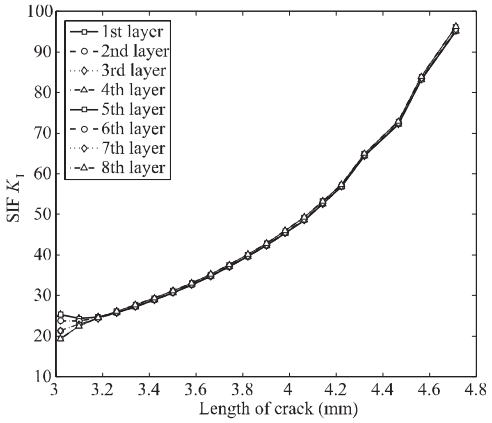

Fig. 24 Variation of SIF versus the crack size for the rectangular isotropic plates with an edge crack and elliptic delamination

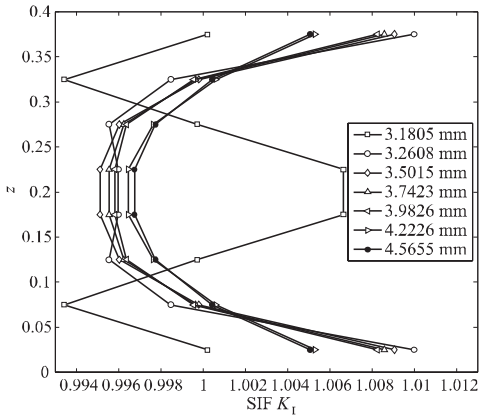

Fig. 25 Distribution of SIF along the thickness direction as the crack growing for the rectangular isotropic plates with an edge crack and elliptic delamination

The material properties of the rectangular composite plate with delamination and transverse crack are the same as those given in Section 8.2.2. Three kinds of stacking sequences $[30]_8$, $[45]_8$ and $[60]_8$ are considered. The boundary

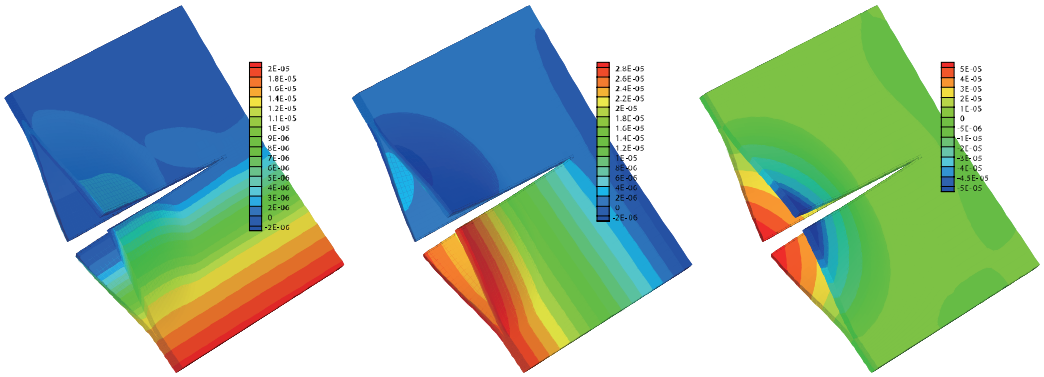

(a) (b) (c)

Fig. 26 Fringe of displacements for the rectangular isotropic plates with an edge crack and elliptic delamination (a) u_1; (b) u_2 and (c) u_3

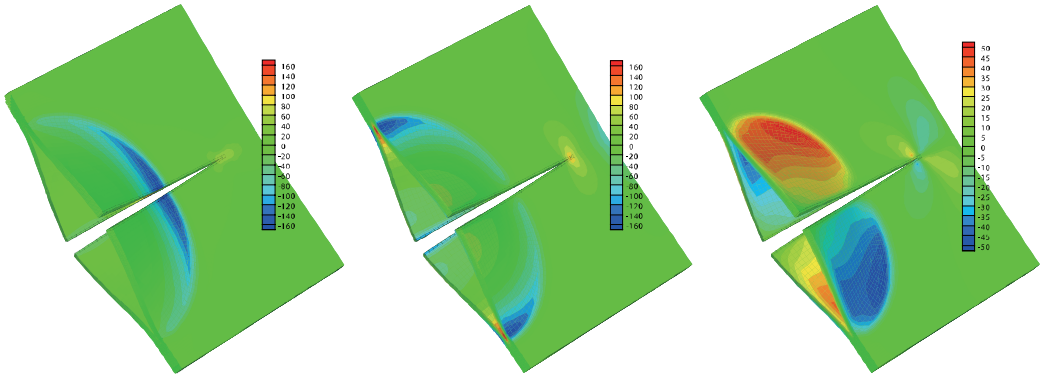

(a) (b) (c)

Fig. 27 Fringe of stresses for the rectangular isotropic plates with an edge crack and elliptic delamination (a) σ_{11}; (b) σ_{22} and (c) σ_{12}

condition and loads are the same as those of the isotropic plate. The elliptic delamination is located at the 4th interface, namely, $[\theta/\theta/\theta/\theta/\cap/\theta/\theta/\theta/\theta]$.

Variation of SIF versus the crack size is shown in Figure 28. The distributions of SIF along the thickness direction are shown in Figure 29 as the crack grows. For fibre angle equal to 45°. K_{I} increases with the crack length. Meanwhile, K_{II} first increases and then decreases as the crack grows. Similar to the isotropic plate, the delamination front significantly affects the crack tip stress field. Both K_{I} and K_{II} along the thickness direction are symmetrical with respect to the mid-plane. The changes in K_{I} and K_{II} along the thickness direction increase as the transverse crack tip approaches the delamination front.

Displacement and stress contours are shown in Figures 30 and 31, respectively, which can illustrate the effect of fibre angle on the displacement and

stress distributions with respect to those of the isotropic plate. Stress concentrations still appear at the transverse crack tip and delamination front. However, in the delamination front, the concentration area of σ_{11} is located at the directions $\omega = -30°$, the concentration area of σ_{22} is located at the directions $\omega = -45°$ and $\omega = 90°$ and the concentration area of σ_{12} is located at region near the directions $\omega = \pm 45°$.

For three kinds of fibre angle ($\theta = 30°$, $\theta = 45°$ and $\theta = 60°$), growth paths are shown in Figure 32.

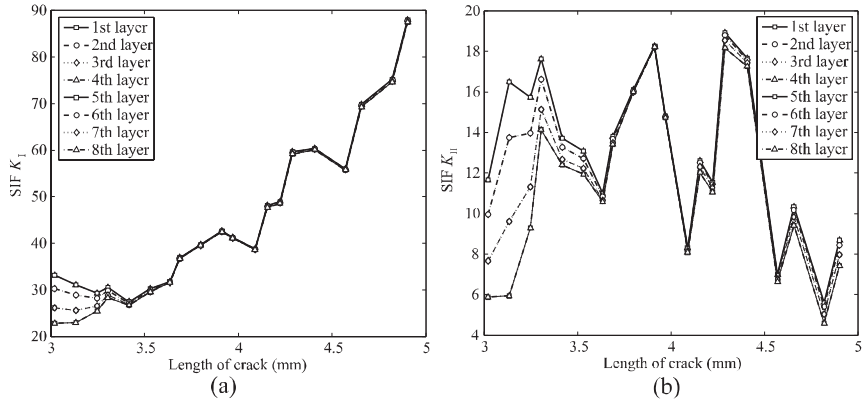

Fig. 28 Variation of SIF versus the crack size for the rectangular composite plates with an edge crack and elliptic delamination

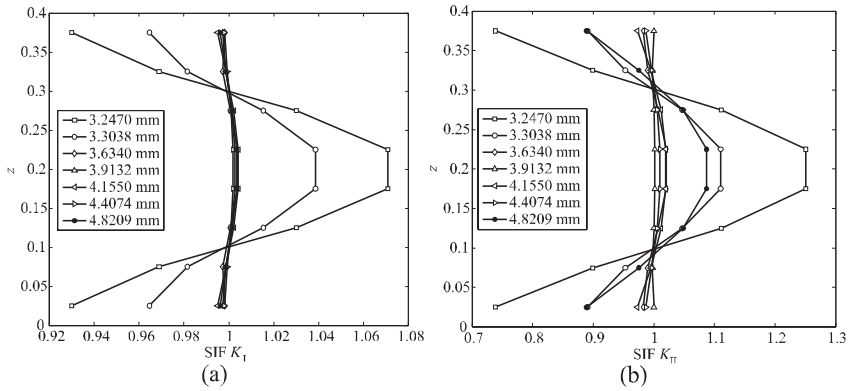

Fig. 29 Distribution of SIF along the thickness direction as the crack grows for the rectangular composite plate with an edge crack and an semi-elliptic delamination (a) K_{I}; (b) K_{II}

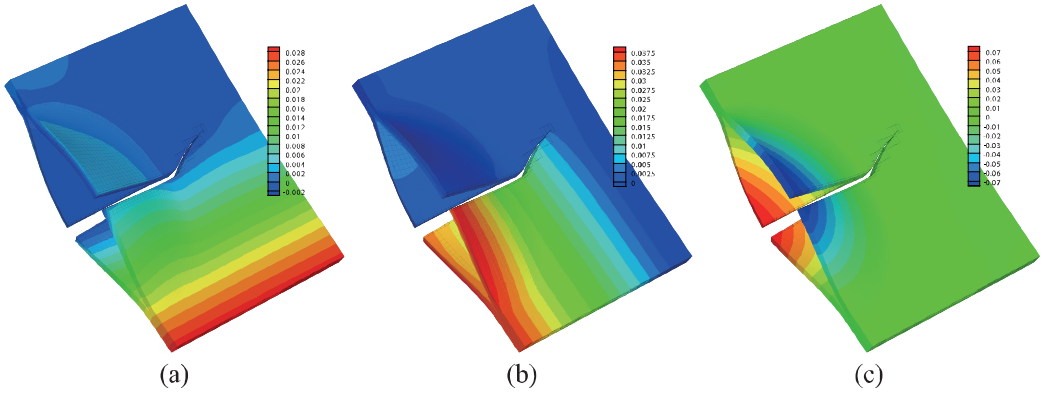

Fig. 30 Fringe of displacements for the rectangular composite plates with an edge crack and an semi-elliptic delamination (a) u_1; (b) u_2 and (c) u_3

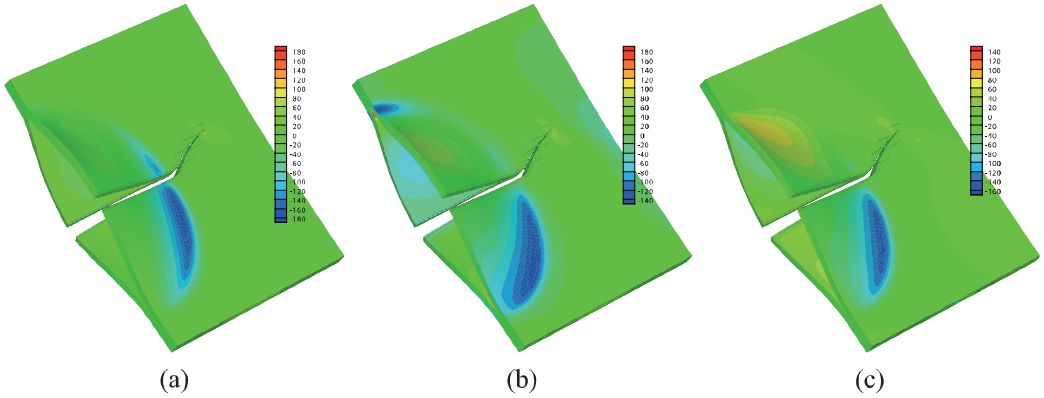

Fig. 31 Fringe of stresses for the rectangular composite plates with an edge crack and elliptic delamination (a) σ_{11}; (b) σ_{22} and (c) σ_{12}

9 Conclusions

Using an improved layerwise displacement assumption and the extended finite element method (XFEM), a new analysis method is proposed for the laminated composite plates with transverse transverse cracks and/or multiple delaminations. The SIF and the crack growth are predicted by the interaction integral method and the maximum circumferential tensile criterion, respectively.

The extended layerwise method (XLWM) of laminated composite plates can not only describe the multiple delaminations together with through and non-through transverse cracks but also accurately predict the displacement and stress fields of the crack tip and delamination front. As the XLWM is quasi three dimensional and the transverse cracks of each single layer are independently described, the thickness distribution of the SIF can be calculated and the predict crack growth angle can be different for each mathematic layer.

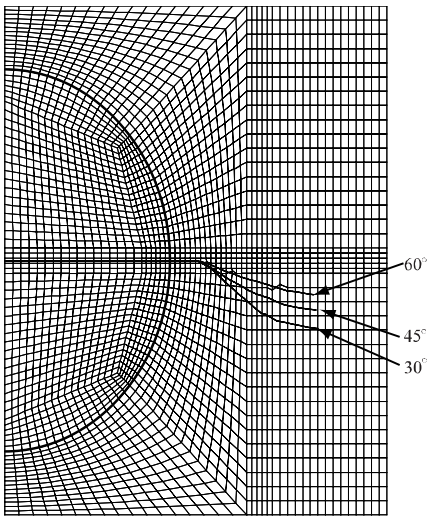

Fig. 32 Growth path for different fibre angle

This is an important advantage compared with the existing shell elements enriched by XFEM. The XLWM extends the application of the XFEM in damage analysis and prediction to laminated composite structures.

The predicted static responses, SIF and crack growth are in excellent agreement to the analytical and the available solutions. From the numerical investigations, the following conclusions can be drawn:

1. Some nodes will be very close to the crack surface as the crack grows. The present local remeshing scheme can shift these nodes without scarifying the mesh quality.
2. For the static response, the present displacement prediction agrees well to that of the 3D elastic prediction of MSC.Nastran whilst the SIF and crack angle predictions are in excellent agreement with the analytical or other reference solutions.
3. The boundary and loading conditions are symmetric with respect to the mid-plane in the numerical example, the thickness distribution of K_{I} follows. Furthermore, K_{I} and K_{II} are always equal to their respective average values along the thickness direction near $z/H \approx 0.2$ and $z/H \approx 0.8$.
4. The delamination front has a profound effect on the crack tip stress field. The changes in K_{I} and K_{II} along the thickness direction increase as the transverse crack tip gets closer to the delamination front.

Acknologment

Supported by National Natural Science Foundations of China (11272180 and 11502286), Tsinghua University Initiative Scientific Research Program and the "Blue Sky Young Scholar" plan of Civil Aviation University of China(205003110307).

A The shape functions in the displacements field along the thickness direction

The linear Lagrange interpolation functions ϕ_k can be expressed as

$$\phi_k(z) = \begin{cases} \varphi_k^1 = -\dfrac{\bar{z}_{k-1} - z}{\bar{z}_k - \bar{z}_{k-1}} & \bar{z}_{k-1} \le z \le \bar{z}_k \\ \varphi_k^2 = -\dfrac{z - \bar{z}_{k+1}}{\bar{z}_{k+1} - \bar{z}_k} & \bar{z}_k \le z \le \bar{z}_{k+1} \end{cases} \tag{40}$$

where $\bar{z}_0 = z_1, \cdots, \bar{z}_k = \frac{z_k + z_{k+1}}{2}, \cdots, \bar{z}_{N+1} = z_{N+1}$. z_k are defined in Figure 1.

The weak discontinuous shape function Θ_k can be expressed as

$$\Theta_k = \begin{cases} -\varphi_k^1 \dfrac{\bar{z}_{k-1} - z}{\bar{z}_{k-1} - z_{k-1}} & \bar{z}_{k-1} \le z \le z_k \\ -\varphi_k^1 \dfrac{z - \bar{z}_k}{\bar{z}_k - z_k} & z_k \le z \le \bar{z}_k \\ -\varphi_k^2 \dfrac{\bar{z}_k - z}{\bar{z}_k - z_k} & \bar{z}_k \le z \le z_{k+1} \\ -\varphi_k^2 \dfrac{z - \bar{z}_{k+1}}{\bar{z}_{k+1} - z_{k+1}} & z_{k+1} \le z \le \bar{z}_{k+1} \end{cases} \tag{41}$$

The shape function Ξ_k used to model delaminations can be expressed as

$$\Xi_k = \begin{cases} -\dfrac{\bar{z}_{k-1} - z}{\bar{z}_{k-1} - z_{k-1}} & \bar{z}_{k-1} \le z \le z_k \\ \dfrac{z - \bar{z}_{k+1}}{\bar{z}_{k+1} - z_{k+1}} & z_{k+1} \le z \le \bar{z}_{k+1} \\ 0 & \text{else} \end{cases} \tag{42}$$

References

1. D. Li, Y. Liu, X. Zhang, International Journal for Numerical Methods in Engineering (2014)
2. S. Joshi, C. Sun, Journal of Composite Materials **19**(1), 51 (1985)
3. A.L. Highsmith, K.L. Reifsnider, Damage in composite materials, ASTM STP **775**, 103 (1982)
4. N. Laws, G.J. Dvorak, M. Hejazi, Mechanics of Materials **2**(2), 123 (1983)
5. N. Laws, G.J. Dvorak, Journal of Composite Materials **22**(10), 900 (1988)
6. A. Wang, P. Chou, S. Lei, Journal of Composite Materials **18**(3), 239 (1984)
7. J. Aboudi, Engineering Fracture Mechanics **26**(5), 637 (1987)
8. P. Gudmundson, Z. Weilin, International Journal of Solids and Structures **30**(23), 3211 (1993)
9. H.Y. Choi, R. Downs, F.K. Chang, Journal of Composite Materials **25**(8), 992 (1991)
10. H. Choi, F. Chang, Journal of Composite Materials **26**(14), 2134 (1992)
11. T.K. O'Brien, Delamination and debonding of materials, ASTM STP **876**, 282 (1985)
12. L. Dharani, H. Tang, International Journal of Fracture **46**(2), 123 (1990)
13. J. Nairn, S. Hu, International Journal of Fracture **57**(1), 1 (1992)
14. J.M. Berthelot, J.F. Le Corre, Composites Science and Technology **60**(7), 1055 (2000)
15. M.J. Swindeman, A regularized extended finite element method for modeling the coupled cracking and delamination of composite materials. Ph.D. thesis, University of Dayton (2011)

16. T. Belytschko, T. Black, International journal for numerical methods in engineering **45**(5), 601 (1999)
17. J. Dolbow, T. Belytschko, Int. J. Numer. Meth. Engng **46**(1), 131 (1999)
18. J. Dolbow, N. Moës, T. Belytschko, Computer Methods in Applied Mechanics and Engineering **190**(51), 6825 (2001)
19. N. Moës, A. Gravouil, T. Belytschko, International Journal for Numerical Methods in Engineering **53**(11), 2549 (2002)
20. N. Sukumar, D. Chopp, B. Moran, Engineering Fracture Mechanics **70**(1), 29 (2003)
21. P. Areias, T. Belytschko, International Journal for Numerical Methods in Engineering **62**(3), 384 (2005)
22. J. Dolbow, N. Moës, T. Belytschko, International Journal of Solids and Structures **37**(48), 7161 (2000)
23. Z. Zhuang, B.B. Cheng, Acta Mechanica Sinica **27**(3), 406 (2011)
24. Z. Zhuang, B. Cheng, Science China Physics, Mechanics and Astronomy **54**(8), 1520 (2011)
25. J.J. Remmers, G.N. Wells, R.d. Borst, International Journal for Numerical Methods in Engineering **58**(13), 2013 (2003)
26. N. Sukumar, Z. Huang, J.H. Prévost, Z. Suo, International Journal for Numerical Methods in Engineering **59**(8), 1075 (2004)
27. T. Hettich, E. Ramm, Computer Methods in Applied Mechanics and Engineering **195**(37), 4753 (2006)
28. T. Nagashima, H. Suemasu, Computers & structures **88**(9), 549 (2010)
29. J. Curiel Sosa, N. Karapurath, Composites Science and Technology **72**(7), 788 (2012)
30. A. Asadpoure, S. Mohammadi, A. Vafai, Thin-Walled Structures **44**(9), 1031 (2006)
31. A. Asadpoure, S.E.F. Mechanics, A. Vafai, Finite Elements in Analysis and Design **42**(13), 1165 (2006)
32. A. Asadpoure, S. Mohammadi, International Journal for Numerical Methods in Engineering **69**(10), 2150 (2007)
33. D. Motamedi, S. Mohammadi, Engineering Fracture Mechanics **77**(17), 3373 (2010)
34. D. Motamedi, S. Mohammadi, International Journal of Mechanical Sciences **54**(1), 20 (2012)
35. E. Barbero, J. Reddy, International Journal of Solids and Structures **28**(3), 373 (1991)
36. A. Chattopadhyay, H. Gu, AIAA journal **32**(8), 1709 (1994)
37. T.O. Williams, International journal of solids and structures **36**(20), 3015 (1999)
38. T.O. Williams, F.L. Addessio, International Journal of Solids and Structures **34**(16), 2003 (1997)
39. M. Cho, J.S. Kim, Journal of applied mechanics **68**(6), 869 (2001)
40. J.S. Kim, M. Cho, International journal for numerical methods in engineering **55**(11), 1323 (2002)
41. J. Reddy, *Mechanics of laminated composite plates and shells: theory and analysis* (CRC press, 2003)
42. M. Stolarska, D. Chopp, International journal of engineering science **41**(20), 2381 (2003)
43. M. Stolarska, D. Chopp, N. Moës, T. Belytschko, International journal for numerical methods in Engineering **51**(8), 943 (2001)
44. S. Mohammadi, *XFEM fracture analysis of composites* (John Wiley & Sons, 2012)
45. J.H. Kim, G.H. Paulino, International Journal for Numerical Methods in Engineering **53**(8), 1903 (2002)
46. S.E. Ashari, S. Mohammadi, in *IOP Conference series: materials science and engineering*, vol. 10 (IOP Publishing, 2010), vol. 10, p. 012240
47. S. Ashari, S. Mohammadi, International Journal for Numerical Methods in Engineering **86**(13), 1507 (2011)
48. S.E. Ashari, S. Mohammadi, Journal of Composite Materials **46**(11), 1367 (2012)
49. Z. Zhuang, Z. Liu, B. Cheng, J. Liao, *Extended Finite Element Method: Tsinghua University Press Computational Mechanics Series* (Academic Press, 2014)
50. V. Saouma, M. Ayari, D. Leavell, Engineering Fracture Mechanics **27(2)**, 171 (1987)
51. J. Dolbow, An extended finite element method with discontinuous enrichment for applied mechanics. Master's thesis, Northwestern University (1999)
52. A. Asadpoure, S. Mohammadi, A. Vafai, Thin-Walled Structures **44**(9), 1031 (2006)

53. M. Aliabadi, P. Sollero, Compos. Sci. Technol. **58**, 1697 (1998)
54. S. Ghorashi, S. Mohammadi, S. Sabbagh-Yazdi, Engineeing Fracture Mechanics **78**, 1906 (2011)
55. F. Shi. F. Gao, Y. Yang, Rock and Soil Mechanics **35**(4), 1203 (2014)